
ALMA View of the Circum-nuclear Disk of the Galactic Center; Tidally-disrupted Molecular Clouds falling to the Galactic Center

Masato Tsuboi^{1,2}, Yoshimi Kitamura¹, Kenta Uehara², Takahiro Tsutsumi³, Ryosuke Miyawaki⁴, Makoto Miyoshi⁵, and Atsushi Miyazaki⁶

¹Institute of Space and Astronautical Science, Japan Aerospace Exploration Agency, 3-1-1 Yoshinodai, Chuo-ku, Sagami-hara, Kanagawa 252-5210, Japan

²Department of Astronomy, The University of Tokyo, Bunkyo, Tokyo 113-0033, Japan

³National Radio Astronomy Observatory, Socorro, NM 87801-0387, USA

⁴College of Arts and Sciences, J.F. Oberlin University, Machida, Tokyo 194-0294, Japan

⁵National Astronomical Observatory of Japan, Mitaka, Tokyo 181-8588, Japan

⁶Japan Space Forum, Kanda-surugadai, Chiyoda-ku, Tokyo, 101-0062, Japan

*E-mail: tsuboi@vsop.isas.jaxa.jp

Received (09-May-2018); Accepted (20-June-2018)

Abstract

We present the high angular resolution and high sensitivity images of the ‘‘Circum-Nuclear Disk (CND)’’ and its surrounding region of Milky Way Galaxy in the CS $J = 2 - 1$, SiO $v = 0$ $J = 2 - 1$, H^{13}CO^+ $J = 1 - 0$, C^{34}S $J = 2 - 1$, and CH_3OH $J_{K_a, K_c} = 2_{1,1} - 1_{1,0} A_{--}$ emission lines using ALMA. The CND is recognized as a torus-like molecular gas with gaps in these emission lines except for the CH_3OH emission line. The inner and outer radii of the CND are estimated to be $R_{\text{in}} \sim 1.5$ and $R_{\text{out}} \sim 2$ pc, respectively. The velocities of the rotation and radial motion are estimated to be $V_{\text{rot}} \sim 115$ km s⁻¹ and $V_{\text{rad}} \sim 23$ km s⁻¹, respectively. The LTE molecular gas mass is estimated to be $M_{\text{LTE}} \sim 3 \times 10^4 M_{\odot}$. We also found some anomalous molecular clouds in the surrounding region. One of the molecular clouds is positionally connected to a part of the CND adjacent to the ‘‘Western Arc’’. However, the cloud is seen to rotate in the opposite direction to the CND. The molecular cloud would be falling currently from the outer region to

the CND and being disrupted by the tidal shear of Sagittarius A*(Sgr A*) because the velocity is not yet assimilated into that of the CND. Another molecular cloud is continuously connected to the tip of the “Eastern Arm (EA)”. The velocity of this cloud is consistent with that of the ionized gas in the EA. These facts suggest that the molecular cloud is falling from the outer region to the vicinity of Sgr A*, being disrupted by the tidal shear, and ionized by strong UV emission from the Central Cluster because the impact parameter of the cloud is smaller than the first cloud. These falling clouds would play an important role in transferring material from the outer region to the CND and/or the vicinity of Sgr A*.

Key words: accretion:accretion disks₁—Galaxy: center₂ — stars: formation₃ — ISM: molecules₄

1 Introduction

The Galactic Center is the nuclear region of the nearest spiral galaxy, Milky Way Galaxy. Sagittarius A* (Sgr A*) is a counterpart of the Galactic Center Black Hole (GCBH) in the regime from radio to X-ray, which is located very near the dynamical center of the galaxy (Reid et al. 2003) and has a mass of $\sim 4 \times 10^6 M_{\odot}$ (e.g. Ghez et al. 2008; Gillessen et al. 2009; Boehle et al. 2016). The “Circum-Nuclear Disk (CND)” has been identified conventionally as a torus-like molecular gas around Sgr A*, which is easily observed by high- J molecular emission lines and dust continuum (e.g. Güsten et al. 1987; Jackson et al. 1993; Marr, Wright, & Backer 1993; Christopher et al. 2005; Montero-Castaño et al. 2009; Martín et al. 2012). The overall kinematics of the CND had been interpreted as rotation around Sgr A* with a velocity of $\sim 100 \text{ km s}^{-1}$. However, the recently observed kinematics of the CND has not been fully explained only by the rotation (e.g. Jackson et al. 1993; Christopher et al. 2005; Shukla, Yun & Scoville 2004; Montero-Castaño et al. 2009; Martín et al. 2012). It is yet considerably controversial how the molecular gas is supplied to the CND (e.g. Montero-Castaño et al. 2009; Takekawa, Oka & Tanaka 2017; Hsieh et al. 2017). Another prominent structure in the vicinity of Sgr A* is the “Galactic Center Mini-spiral (GCMS)”, which is a bundle of the ionized gas streams orbiting around Sgr A* (e.g. Lacy et al. 1980; Ekers et al. 1983; Lo & Claussen 1983; Serabyn & Lacy 1985; Serabyn et al. 1988; Lacy, Achtermann, & Serabyn 1991; Roberts, Yusef-Zadeh, & Goss 1996; Scoville et al. 2003; Zhao et al. 2009; Zhao et al. 2010; Tsuboi et al. 2017) and is likely feeding the GCBH. There remains considerable controversy about the origin and life time of the GCMS. The relation between these structures is yet an open question although the

GCMS is located along the inner ridge of the CND.

The CND itself had been observed intensively by the existing millimeter interferometers and IR telescopes as mentioned above, while the outer region surrounding the CND had not been sufficiently observed because of their insufficient sensitivities and small field of view. In addition, the molecular gas in the outer region would be detected better in low- J molecular emission lines because of their lower excitation (e.g. Wright et al. 2001) although the CND itself is prominent in high- J molecular emission lines. The Atacama Large Millimeter/Submillimeter Array (ALMA) can detect both the CND itself and the molecular gas in the outer surrounding region because ALMA has an unprecedented high sensitivity compared to previous telescopes. The more detailed gas kinematics of the wider area including the CND must provide key information to address the issues above mentioned. Therefore, we have observed the molecular gas in the wider region using ALMA.

The distance to the Galactic Center is assumed to be 8 kpc in this paper (e.g. Ghez et al. 2008; Gillessen et al. 2009; Schödel, Merritt, & Eckart 2009; Boehle et al. 2016). Then, $1''$ corresponds to about 0.04 pc at the distance. We use the Galactic coordinates. The directions used in this paper, for example “north”, “south”, are referred to the Galactic coordinates. We also use the traditional nomenclature of the substructures of the GCMS because it had been established although it had been named referring to the equatorial coordinates.

2 Observation and Data Reduction

We have produced a 136 pointing mosaic of the 12-m array and a 68 pointing mosaic of the 7-m array (ACA) which cover a $330'' \times 330''$ area including the CND and the “Galactic Center 50 km s⁻¹ Molecular Cloud (50MC)”, a most conspicuous star forming region in the vicinity of Sgr A*, in the CS $J = 2 - 1$ (97.980953 GHz), SiO $v = 0 J = 2 - 1$ (86.846995 GHz), H¹³CO⁺ $J = 1 - 0$ (86.754288 GHz), C³⁴S $J = 2 - 1$ (96.41950 GHz), and CH₃OH $J_{K_a, K_c} = 2_{1,1} - 1_{1,0} A_{--}$ (97.582808 GHz) emission lines in ALMA Cy.1 (2012.1.00080.S, PI Tsuboi, M.). The CS $J = 2 - 1$ and H¹³CO⁺ $J = 1 - 0$ emission lines are dense molecular gas tracers with $n(\text{H}_2) \gtrsim 10^4 \text{ cm}^{-3}$ and $n(\text{H}_2) \gtrsim 10^5 \text{ cm}^{-3}$, respectively. The C³⁴S $J = 2 - 1$ emission line also traces the dense gas with $n(\text{H}_2) \gtrsim 10^4 \text{ cm}^{-3}$, but is expected to be optically thin even in the region in contrast to the optically thick CS $J = 2 - 1$ emission line. The SiO $J = 2 - 1$ emission line is a tracer of strong C-shock with $\Delta V \gtrsim 30 \text{ km s}^{-1}$ in molecular clouds (e.g. Gusdorf et al. 2008; Jiménez-Serra et al. 2008), while the CH₃OH emission line is known as a tracer of weak shocks ($\Delta V \sim 10 \text{ km s}^{-1}$) (e.g. Hartquist et al. 1995). The frequency range in our observation also includes the H42 α recombination line (85.6884 GHz) which is a tracer of ionized gas (e.g. Tsuboi et al. 2017).

The resultant maps have angular resolutions of $(2''.3 - 2''.5) \times (1''.6 - 1''.8)$, $PA \sim -30^\circ$ using “natural weighting” sampling on the spatial frequency ($u - v$) plane, which corresponds to $(0.09 - 0.10)\text{pc} \times (0.06 - 0.07)\text{pc}$ at the Galactic center distance. The synthesized beams of this observation are approximately 4 times smaller than those of previous molecular line observations (e.g. Montero-Castaño et al. 2009; Martín et al. 2012). The original velocity resolution is 1.7 km s^{-1} (488 kHz). J0006-0623, J1517-2422, J717-3342, J1733-1304, J1743-3058, J1744-3116 and J2148+0657 were used as phase calibrators. The flux density scale was determined using Titan, Neptune and Mars. The calibration and imaging of the data were performed by CASA (McMullin et al. 2007). We made the spectral line images with $\Delta V = 5 \text{ km s}^{-1}$ of the emission lines mentioned above. The rms noise levels of the resultant maps are $\sim 0.002 \text{ Jy/beam} \times 5 \text{ km s}^{-1}$ or $\sim 0.35 \text{ K km s}^{-1}$. Because the observation has a large time span of one year and seven months, the flux uncertainty is as large as 15 %. We will present the full data of the observation and the analysis about 50MC in another coming paper (Uehara et al. submitted).

For comparison, we analyzed the mosaic observation data of the CND with ALMA in the CS $J = 7 - 6$ (342.882857 GHz) emission line obtained from the JVO portal of NAOJ (ALMA#2012.1.00543.S). The data of the CS $J = 7 - 6$ emission line have an angular resolution of $4''.3 \times 2''.7$, $PA \sim -35^\circ$ using “natural weighting” sampling on the $u - v$ plane, which corresponds to $0.17\text{pc} \times 0.11\text{pc}$ at the Galactic center distance. The analysis of the data were also performed by CASA.

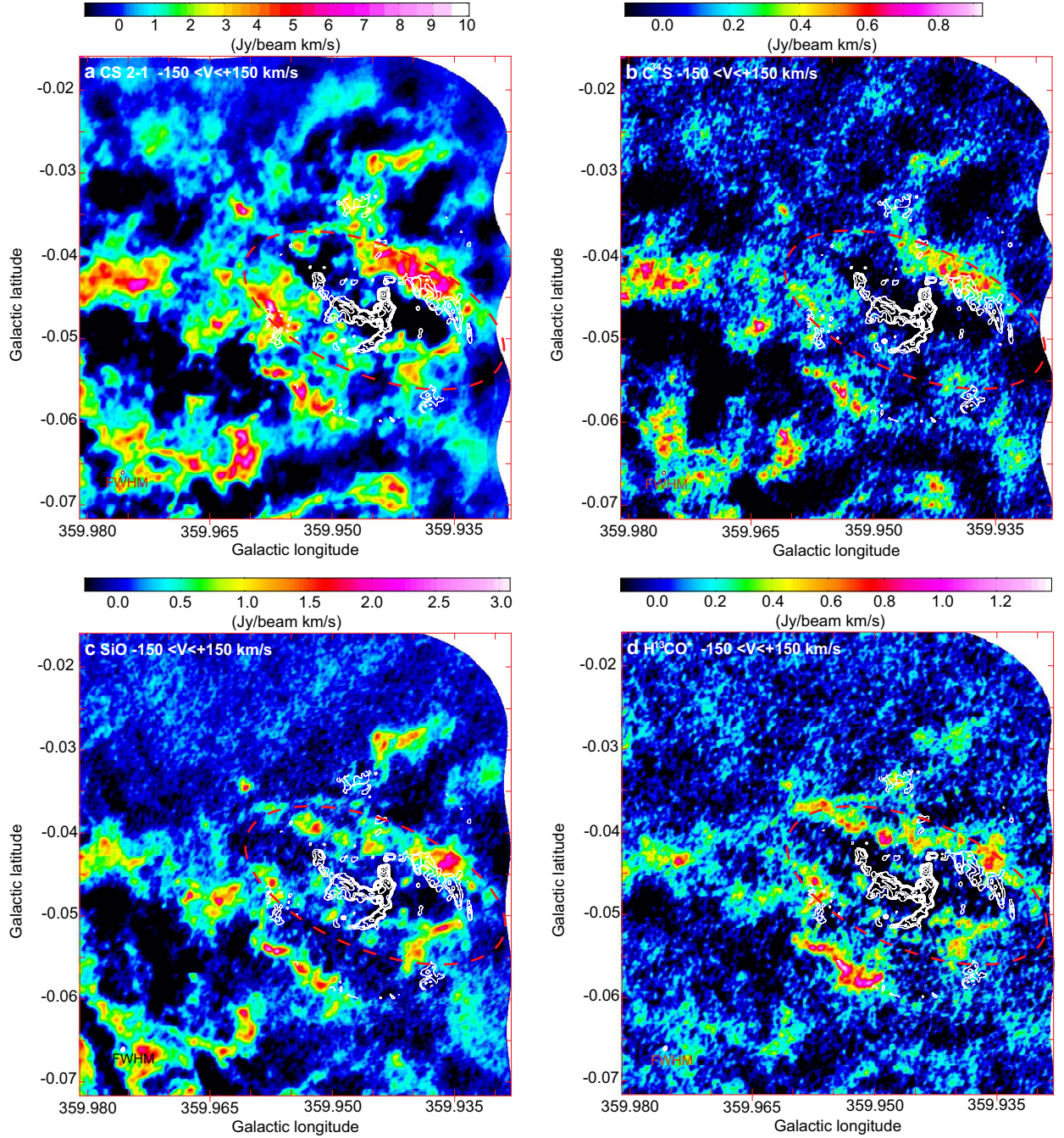


Fig. 1. Integrated intensity (moment 0) maps of the CND (red dashed ellipse shows the elliptical outline of the CND with an assumed radius = $58''$, $PA = 67^\circ$, and inclination = 30°) and the surrounding region in the **a** CS $J = 2 - 1$, **b** C³⁴S $J = 2 - 1$, **c** SiO $v = 0$, $J = 2 - 1$, **d** H¹³CO⁺ $J = 1 - 0$, **e** CH₃OH $J_{K_a, K_c} = 2_{1,1} - 1_{1,0} A - -$, and **f** H42 α emission lines. The integrated velocity range is $V_{LSR} = -150$ to 150 km s⁻¹. The FWHM beam sizes are $(2.''3 - 2.''5) \times (1.''6 - 1.''8)$, $PA \sim -30^\circ$ shown at the lower left corners of the panels as ovals. The contours in each panel show the continuum emission at 100 GHz of the “Galactic Center Mini-spiral” for comparison (Tsuboi et al. 2016). They are set at 3.75, 7.5, 15, 30, 60, 120, 240, 480, and 960 mJy beam⁻¹. **g** Integrated intensity (moment 0) map in the CS $J = 7 - 6$ emission line is shown. The data has an angular resolution of $4.''6 \times 2.''7$, $PA \sim -35^\circ$. **h** Continuum map at 670 GHz, which was obtained from the JCMT Archive. The data has an angular resolution of $8''$.

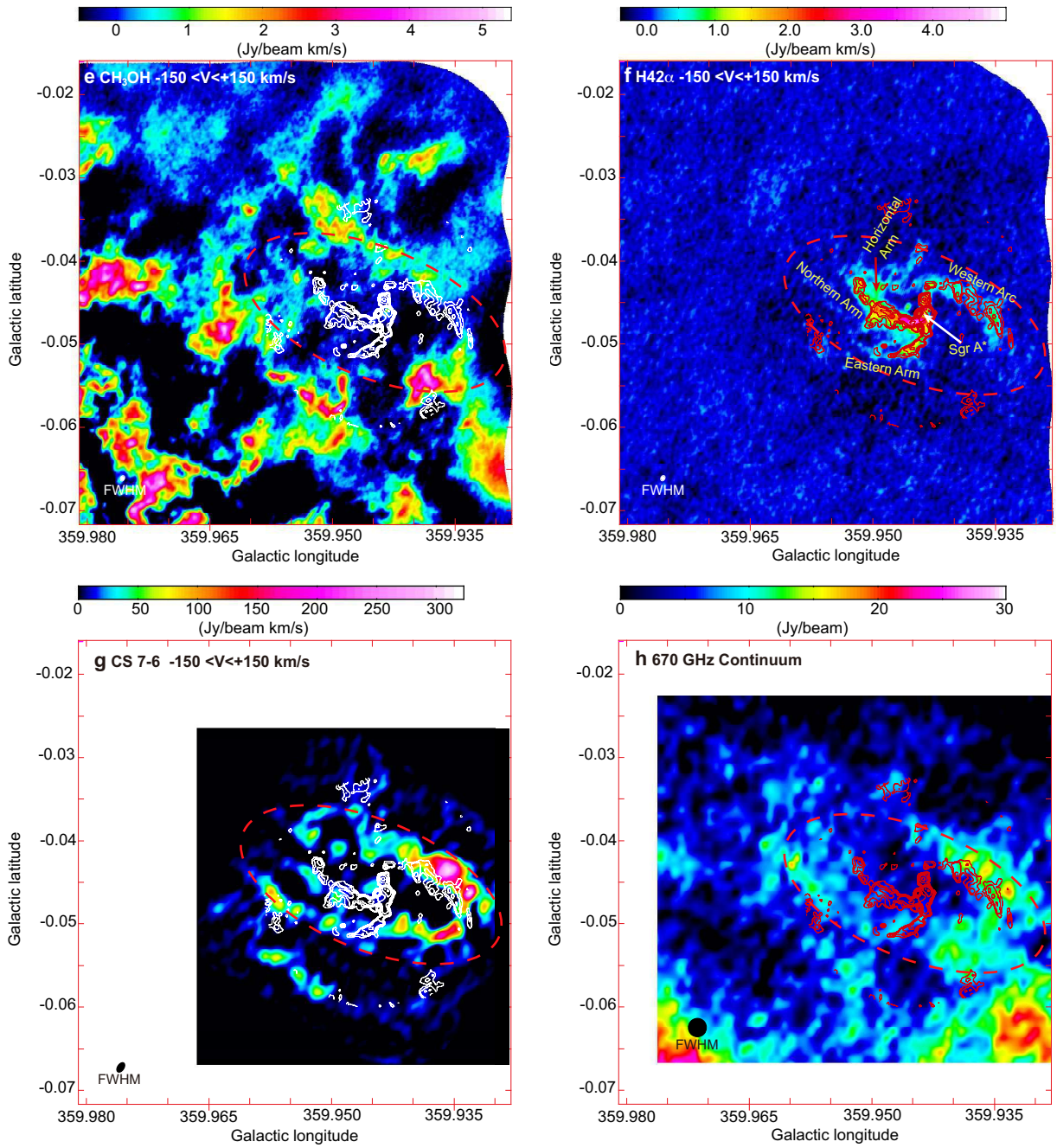


Fig. 1. Continued.

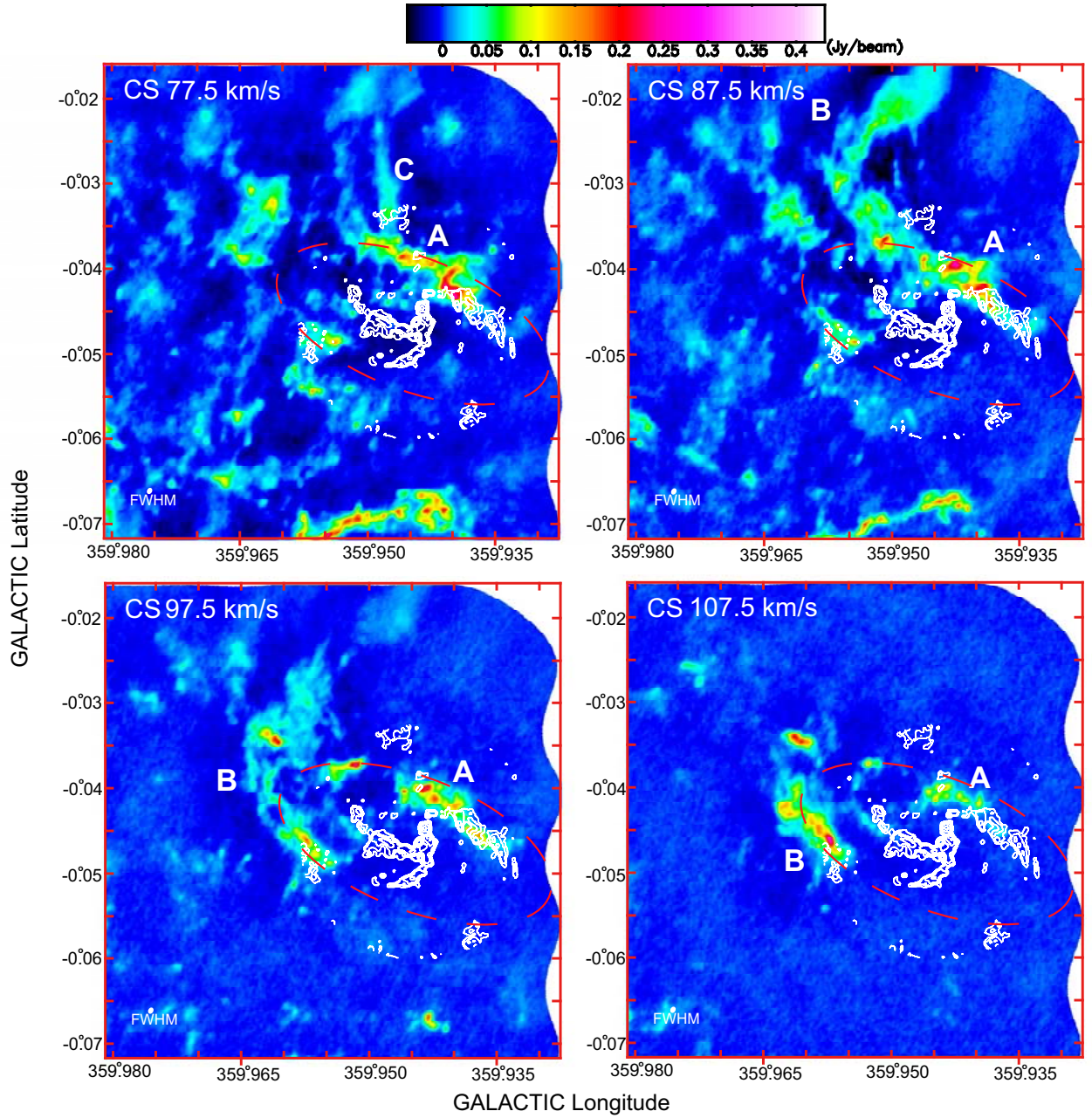


Fig. 2. Channel maps of the CND (red-dashed ellipse) and its surrounding region in the CS $J = 2 - 1$ emission line. The central velocity range is from $V_{\text{c,LSR}} = -142.5$ to $+147.5$ km s^{-1} , and the velocity width of each panel is 10 km s^{-1} . The angular resolution is $2''.3 \times 1''.6$ in FWHM, which is shown as the oval at the lower left corner of each panel. The contours in the figure show the continuum emission of the “Galactic Center Mini-spiral (GCMS)” at 100 GHz for comparison (Tsuboi et al. 2016). They are set at $3.75, 7.5, 15, 30, 60, 120, 240, 480,$ and 960 mJy beam^{-1} . The remaining panels are in <http://www.vsop.isas.jaxa.jp/~nakahara/tsuboi>.

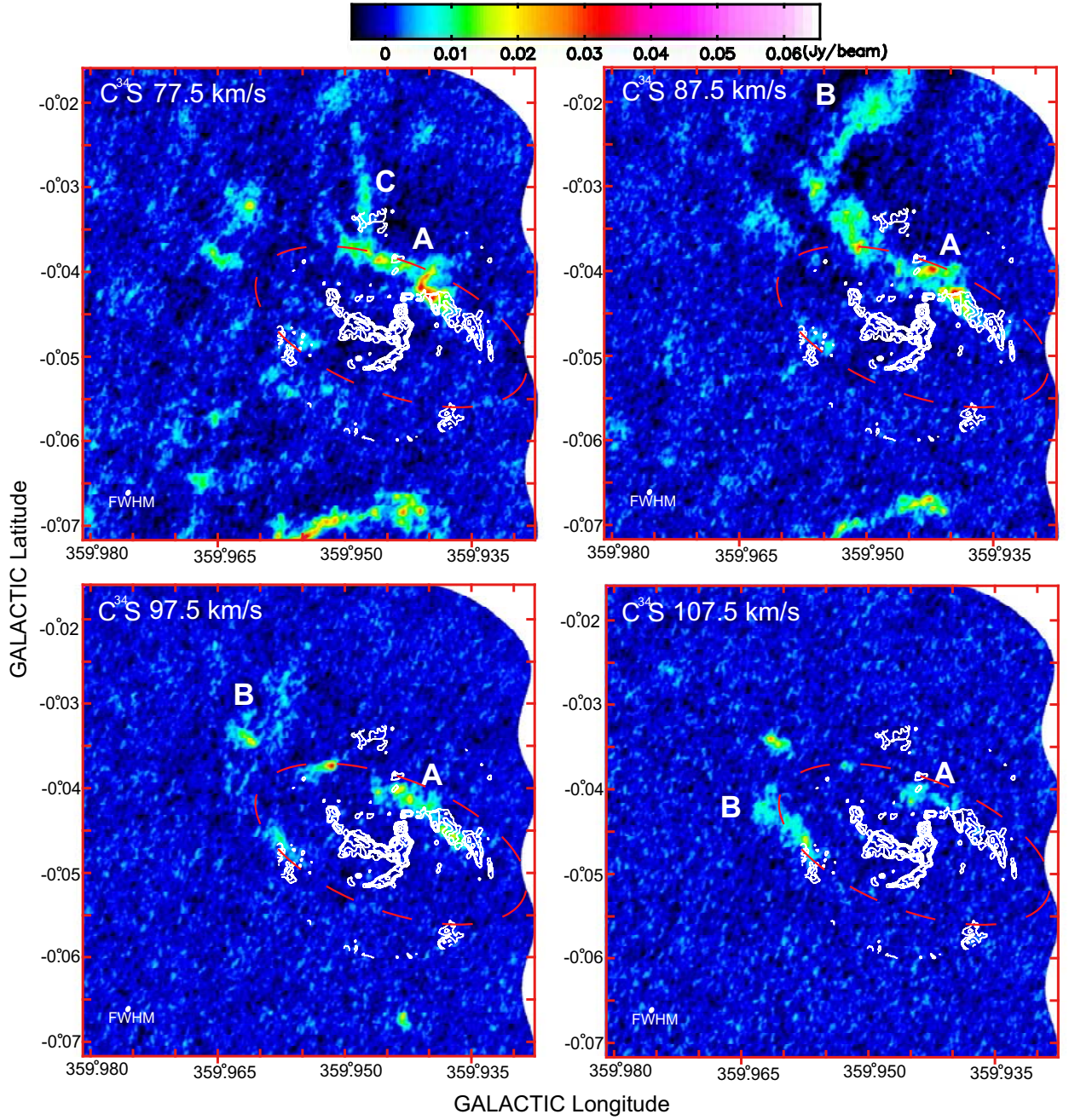


Fig. 3. Channel maps of the CND (red-dashed ellipse) and its surrounding region in the $\text{C}^{34}\text{S } J = 2 - 1$ emission line. The central velocity range is from $V_{e, \text{LSR}} = -142.5$ to $+147.5 \text{ km s}^{-1}$, and the velocity width of each panel is 10 km s^{-1} . The angular resolution is $2''.3 \times 1''.7$ in FWHM, which is shown as the oval at the lower left corner of each panel. The contours in the figure show the continuum emission of the “Galactic Center Mini-spiral (GCMS)” at 100 GHz for comparison (Tsuboi et al. 2016). They are set at 3.75, 7.5, 15, 30, 60, 120, 240, 480, and 960 mJy beam^{-1} . The remaining panels are in <http://www.vsop.isas.jaxa.jp/~nakahara/tsuboi>.

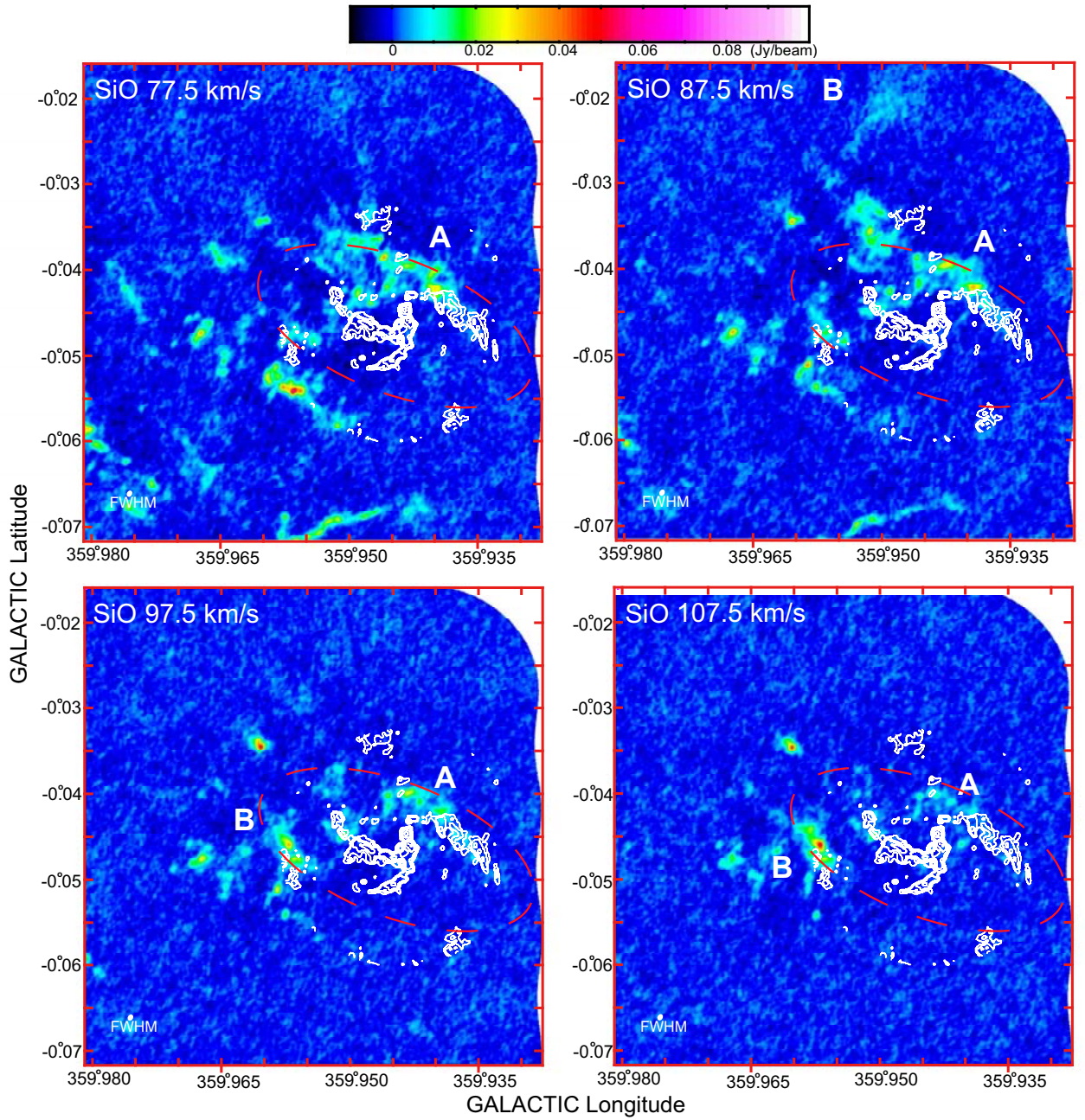


Fig. 4. Channel maps of the CND (red-dashed ellipse) and its surrounding region in the SiO $v = 0, J = 2 - 1$ emission line. The central velocity range is from $V_{c,LSR} = -142.5$ to $+147.5$ km s $^{-1}$, and the velocity width of each panel is 10 km s $^{-1}$. The angular resolution is $2''.5 \times 1''.8$ in FWHM, which is shown as the oval at the lower left corner of each panel. The contours in the figure show the continuum emission of the “Galactic Center Mini-spiral (GCMS)” at 100 GHz for comparison (Tsuboi et al. 2016). They are set at 3.75, 7.5, 15, 30, 60, 120, 240, 480, and 960 mJy beam $^{-1}$. The remaining panels are in <http://www.vsoop.isas.jaxa.jp/~nakahara/tsuboi>.

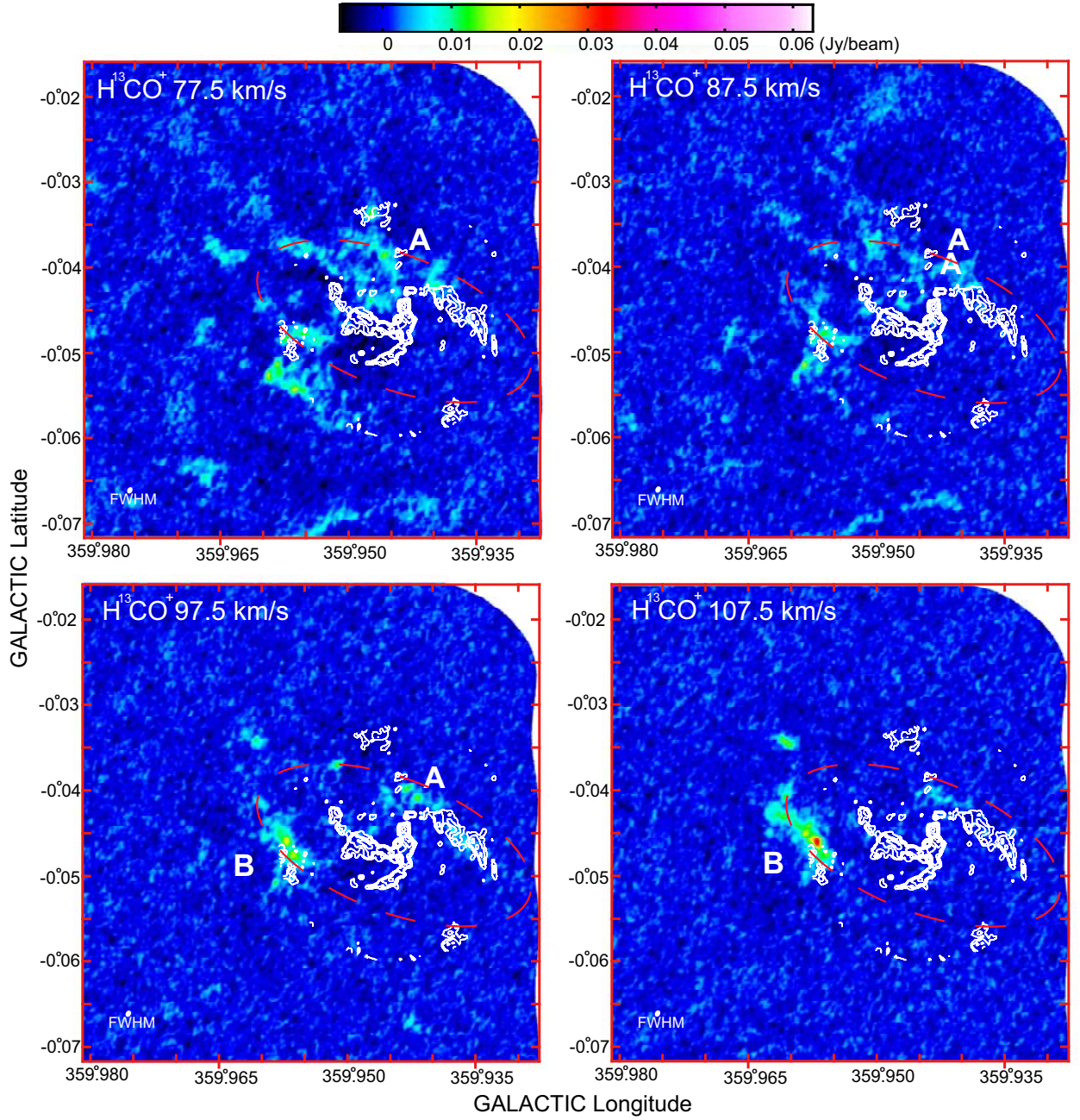


Fig. 5. Channel maps of the CND (red-dashed ellipse) and its surrounding region in the H^{13}CO^+ $J = 1 - 0$ emission line. The central velocity range is from $V_{\text{c,LSR}} = -142.5$ to $+147.5$ km s^{-1} , and the velocity width of each panel is 10 km s^{-1} . The angular resolution is $2''.5 \times 1''.8$ in FWHM, which is shown as the oval at the lower left corner of each panel. The contours in the figure show the continuum emission of the “Galactic Center Mini-spiral (GCMS)” at 100 GHz for comparison (Tsuboi et al. 2016). They are set at $3.75, 7.5, 15, 30, 60, 120, 240, 480,$ and 960 mJy beam^{-1} . The remaining panels are in <http://www.vsop.isas.jaxa.jp/~nakahara/tsuboi>.

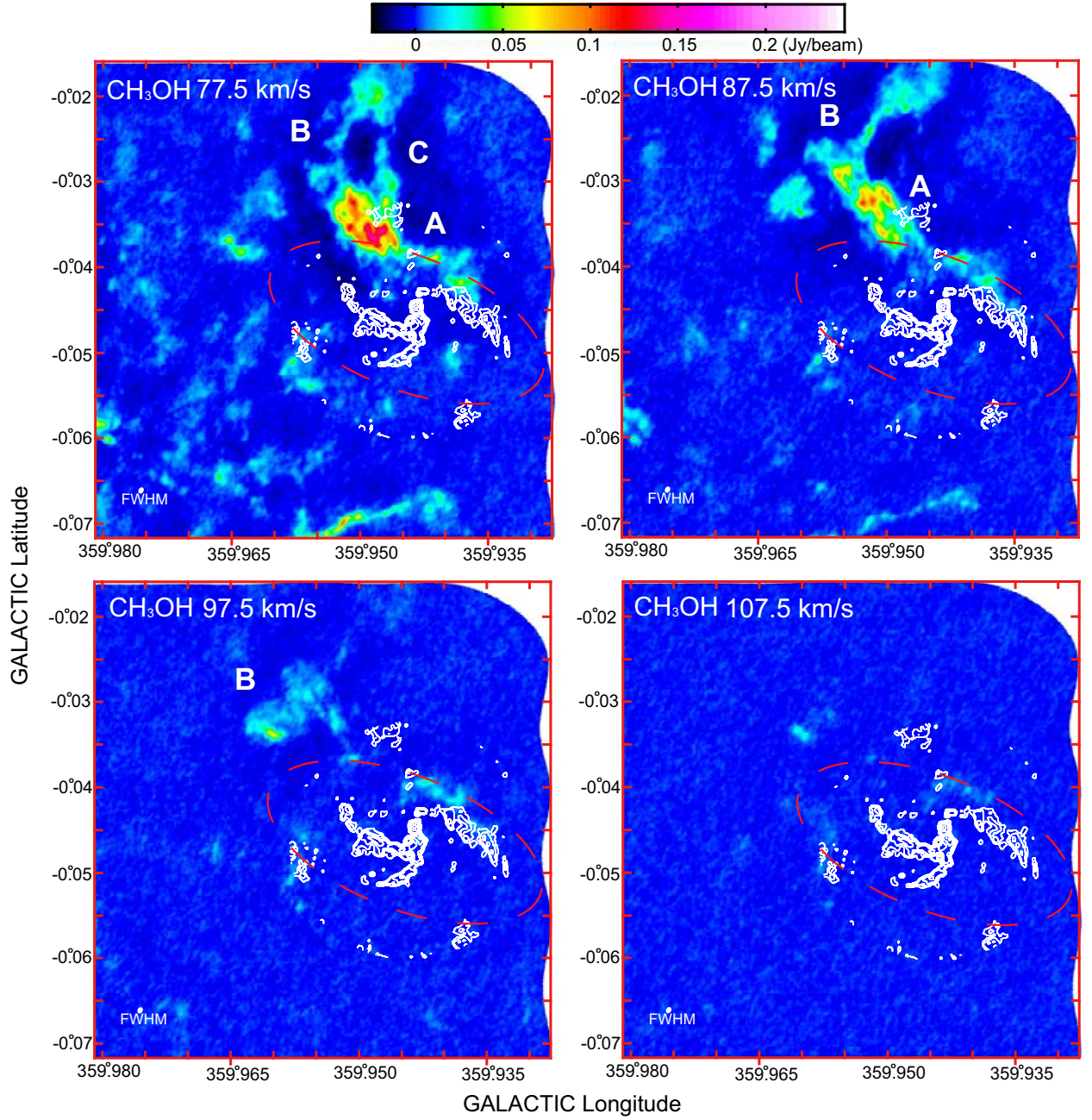


Fig. 6. Channel maps of the CN D (red-dashed ellipse) and its surrounding region in the CH_3OH emission line. The central velocity range is from $V_{\text{c,LSR}} = -142.5$ to $+147.5$ km s^{-1} , and the velocity width of each panel is 10 km s^{-1} . The angular resolution is $2''.3 \times 1''.7$ in FWHM, which is shown as the oval at the lower left corner of each panel. The contours in the figure show the continuum emission of the “Galactic Center Mini-spiral (GCMS)” at 100 GHz for comparison (Tsuboi et al. 2016). They are set at 3.75 , 7.5 , 15 , 30 , 60 , 120 , 240 , 480 , and 960 mJy beam^{-1} . The remaining panels are in <http://www.vsop.isas.jaxa.jp/~nakahara/tsuboi>.

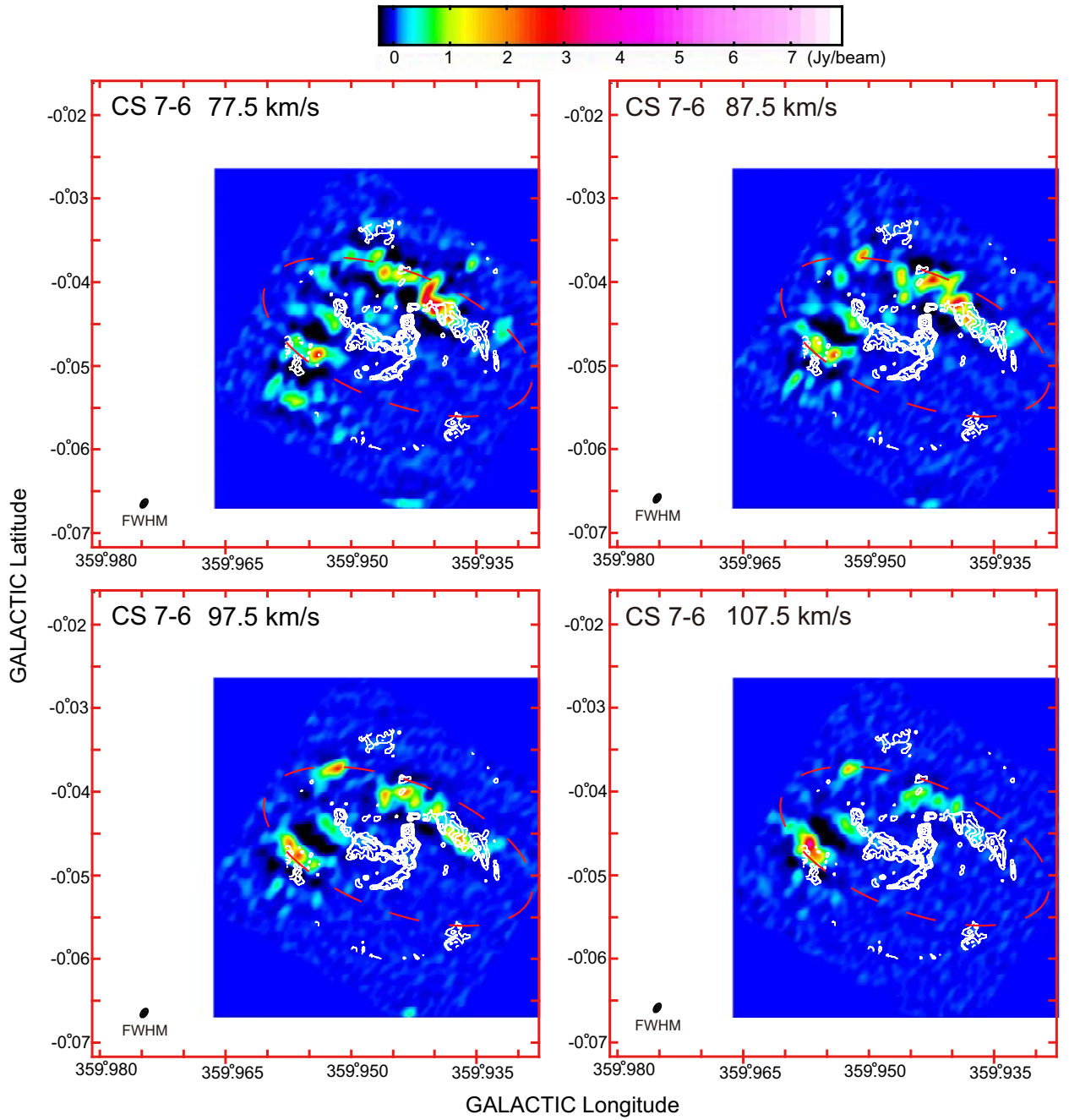


Fig. 7. Channel maps of the CND (red-dashed ellipse) and its surrounding region in the CS $J = 7 - 6$ emission line. The central velocity range is from $V_{c,LSR} = -142.5$ to $+147.5$ km s^{-1} , and the velocity width of each panel is 10 km s^{-1} . The angular resolution is $4''.6 \times 2''.7$ in FWHM, which is shown as the oval at the lower left corner of each panel. The contours in the figure show the continuum emission of the “Galactic Center Mini-spiral (GCMs)” at 100 GHz for comparison (Tsuboi et al. 2016). They are set at 3.75, 7.5, 15, 30, 60, 120, 240, 480, and 960 mJy beam $^{-1}$. The remaining panels are in <http://www.vsop.isas.jaxa.jp/~nakahara/tsuboi>.

3 Results

3.1 Integrated Intensity (Moment 0) Maps

Figure 1 shows the integrated intensity (moment 0) maps of the CND (red-dashed ellipse) and its surrounding region in the CS $J = 2 - 1$, C³⁴S $J = 2 - 1$, SiO $v = 0, J = 2 - 1$, H¹³CO⁺ $J = 1 - 0$, and CH₃OH $J_{K_a, K_c} = 2_{1,1} - 1_{1,0} A_{--}$ and H42 α emission lines. The integrated velocity range of the panels is $V_{\text{LSR}} = -150$ to 150 km s⁻¹. Because the previous observations show that the CND has the rotation velocity of $100 - 110$ km s⁻¹ and the random or radial velocity of $10 - 30$ km s⁻¹ (e.g. Güsten et al. 1987; Jackson et al. 1993; Christopher et al. 2005), the integrated velocity range contains almost all of the total velocity extent of the CND. These panels are cut from the large area mosaic data mentioned in the previous section. The contours in the figure show the continuum emission at 100 GHz, which mainly traces the GCMS, for comparison (Tsuboi et al. 2016). Figure 1 also shows the moment 0 map of the CS $J = 7 - 6$ emission line by ALMA and the continuum map at 670 GHz by JCMT for comparison. Although the mosaic map of the CS $J = 7 - 6$ emission line with a similar angular resolution had been obtained by SMA (Montero-Castaño et al. 2009), the sensitivities of our maps are five times or more higher than those of the SMA maps. The CND is identified as a fragmented ring surrounding the GCMS in the CS $J = 2 - 1$, C³⁴S, SiO, and H¹³CO⁺ emission lines (Cf. Montero-Castaño et al. 2009; Martín et al. 2012), and is less prominent in the CH₃OH emission line. Note that the CH₃OH emission line seems to trace the surrounding gas rather than the CND itself. There are many extended components surrounding the CND in the CS $J = 2 - 1$, C³⁴S, SiO, and H¹³CO⁺ lines, whereas the CS $J = 7 - 6$ line and 670 GHz continuum emissions mainly trace the CND.

3.2 Channel Maps

Figures 2, 3, 4, 5, and 6 show the channel maps of the same region of figure 1 with the central velocities of $V_{\text{c,LSR}} = -142.5$ to $+147.5$ km s⁻¹ in the CS, C³⁴S, SiO, H¹³CO⁺, and CH₃OH emission lines, respectively. The velocity width of each panel is 10 km s⁻¹. Figure 7 shows the channel maps with the same velocity range in the CS $J = 7 - 6$ emission line for comparison.

Although the components of the CND identified in these channel maps are roughly consistent with those in the previous observations (e.g. Güsten et al. 1987; Jackson et al. 1993; Marr, Wright, & Backer 1993; Shukla, Yun & Scoville 2004; Montero-Castaño et al. 2009; Martín et al. 2012), significant differences are found in the different emission lines (Cf. Martín et al. 2012). The kinematics of the CND does not always follow a simple rotation law around Sgr A* as mentioned in the Introduction. There is a feature apparently distributed just outside of the “Western Arc” (WA) of the

GCMS (see also figure 1-f). This feature is also prominent in the integrated intensity maps of several previous papers (e.g. Montero-Castaño et al. 2009; Martín et al. 2012). However, the feature has two distinct velocity components with negative and positive radial velocities. The positive velocity component will be discussed separately in Subsection 3.2.1. The negative velocity component is identified in the panels in the CS emission line of $V_{c,LSR} = -142.5$ to $+7.5$ km s⁻¹. The component is also identified in the C³⁴S, SiO, and H¹³CO⁺ emission lines, while the component cannot be identified in the CH₃OH emission line. The peak position of the component is seen to be shifting from west to east along the outer edge of the WA with increasing velocity. The similar velocity shift has been observed for the WA in the H42 α emission line (e.g. Tsuboi et al. 2017). Therefore this component would be physically associated with the WA and follow a simple rotation law around Sgr A*. The component corresponds to the “northwestern sector” of the CND.

Another component is identified on the opposite side of the GCMS in the velocity range of $V_{c,LSR} \sim -82.5$ and $+7.5$ km s⁻¹. This component is seen to be corresponds to the “southwestern sector” of the CND. The peak position of the component would be also shifting from west to east with increasing velocity although the component has no clear association with the ionized gas of the GCMS. The “northwestern sector” and “southwestern sector” form the “western half” of the CND, which is also identified clearly in the CS $J = 7 - 6$ emission line.

Meanwhile, the “eastern half” of the CND has a complicated structure. There are several components with positive radial velocity seen in the eastern area of the CND. However, we should keep in mind that all molecular clouds seen toward the CND do not always belong to it because this is a very overlapping region as shown in Figure 1. The molecular clouds coming from outer regions and intruding into the CND may be molecular gas flows feeding to the CND. On the other hand, the molecular clouds passing the CND from one outer region to another outer region are thought not to belong to the CND even if they are seen toward the CND. The distinction between the CND components and clouds overlapping the CND by chance in the same line of sight is necessary to obtain the true image of the CND.

3.2.1 Anomaly A

The positive velocity component apparently distributed along the WA is prominent in the panels of the CS emission line with $V_{c,LSR} = +67.5$ to $+117.5$ km s⁻¹. The component is also identified in the C³⁴S and SiO emission lines, while it is faint in the H¹³CO⁺ emission line. The “southwestern half” of the component overlaps positionally with the northwestern sector of the CND, as mentioned above. The velocity of the component is different from that of ionized gas in the WA (e.g. Tsuboi et al. 2017). Thus this component would not be physically associated with the WA. The component

also had been identified conventionally as a part of the CND, although the positive radial velocity in the western half of the CND means that the component should rotate oppositely around Sgr A* if it really belongs to the CND. This component is called Anomaly A (AA) hereafter.

AA extends to the northeast in the panels of the CS emission line with $V_{c,LSR} = 67.5$ and 87.5 km s^{-1} (see Figure 2). This seems to cross another component extending from southeast to northwest (Anomaly B, see below) around $l \sim 359.955^\circ, b \sim -0.030^\circ$ in the panel of $V_{c,LSR} = 87.5$ km s^{-1} . In the CH_3OH emission line, the “northeastern half” of the component with $V_{c,LSR} = +77.5$ to $+87.5$ km s^{-1} is prominent especially although the “southwestern half” is faint. Because the CH_3OH emission line is known as a weak shock as mentioned in Section 2, the “northeastern half” seems abundant in mildly shocked molecular gas ($\Delta V \sim 10$ km s^{-1}).

3.2.2 Anomaly B

The panels with $V_{c,LSR} = +87.5$ to $+117.5$ km s^{-1} in the CS emission line show that an elongated molecular cloud seems to approach SgrA* along an arc from the north to the outer end of the Eastern Arm (EA) of the GCMS with increasing velocity (see also figure 1-f). The component is most prominent in the CS emission line and is identified partly in the C^{34}S , SiO , H^{13}CO^+ , and CH_3OH emission lines. The component is appeared to be a bundle of filamentary substructures. Although the component had been identified as a small protrusion from the CND since the early days of the CND observation using the low- J emission lines (e.g. Güsten et al. 1987; Zylka, Mezger, & Wink 1990; Wright et al. 2001), this had never been revealed as the bundle of filamentary substructures by existing telescopes because it is deeply embedded in the CND. Note that the component does not obey the simple rotation law of the CND. The component is called Anomaly B (AB) hereafter. The south end of AB seems to be continuously connected with the EA. On the other hand, the north end of AB is located beyond the CND. The filamentary substructures remarkable in the CS emission line are faint in the SiO and H^{13}CO^+ emission lines except for the contact area between AB and the EA, $l \sim 359.958^\circ, b \sim -0.045^\circ$. This suggests that the strongly shocked molecular gas with $\Delta V \gtrsim 30$ km s^{-1} and $n(\text{H}_2) \gtrsim 10^5$ cm^{-3} is abundant in the contact area. Because the northern half of AB is prominent in the CH_3OH emission line, the northern half seems abundant in mildly shocked molecular gas ($\Delta V \sim 10$ km s^{-1}).

Meanwhile, the southern half of AB is not seen in the CH_3OH emission line. The CH_3OH molecule is reported to be destroyed easily through the cosmic-ray photodissociation reaction in the vicinity of Sgr A*; $\text{CH}_3\text{OH} \rightarrow \text{H}_2\text{CO} + \text{H}_2$ (Harada et al. 2015). This is probably why the CND itself is faint in the CH_3OH emission line. This suggests that the southern half of AB may be located near Sgr A* and the northern half is really farther from it. Similarly, the CH_3OH maps suggest that the

northeastern half of AA is farther from Sgr A* and the southwestern half is located near Sgr A*.

3.2.3 Anomaly C

The panels with $V_{c,LSR} = 77.5 \text{ km s}^{-1}$ in the CS, C³⁴S and CH₃OH emission lines show that a nearly vertical structure is located around $l \sim 359.948^\circ, b \sim -0.032^\circ$ (see Figures 2, 3, and 6). This component is identified faintly in the SiO emission line (see Figure 4), but is not identified in the H¹³CO⁺, and CS $J = 7 - 6$ emission lines. The south end of this component crosses AA. The south end seems to be continuously connected with the Horizontal Arm of the GCMS (see Figure 1-f). The component is called Anomaly C (AC) hereafter.

3.2.4 Anomaly D

The panels with $V_{c,LSR} = -72.5$ to -32.5 km s^{-1} in the CS emission line show that a compact molecular cloud is located around $l \sim 359.948^\circ, b \sim -0.035^\circ$ (see Figure 2). The component is prominent only in the CS emission line. This component is identified partly in the C³⁴S emission line, but is faint in the SiO, H¹³CO⁺, and CH₃OH emission lines (see Figures 3, 4, 5, and 6). The negative radial velocity at the eastern half of the CND means that the component should rotate oppositely around Sgr A* if it belongs to the CND. Because this component is faint in the CH₃OH emission line, the cloud is likely located near Sgr A* as it looks. In addition, the southern edge of the component is detected faintly in the H42 α recombination line (see Figure 1-f). The component is called Anomaly D (AD) hereafter.

3.2.5 -80 km s⁻¹ molecular cloud

The panels with $V_{c,LSR} = -102.5$ to -42.5 km s^{-1} in the CS emission line show that an isolated molecular cloud is located around $l \sim 359.963^\circ, b \sim -0.065^\circ$. This component is also identified in the channel maps of the C³⁴S, SiO, H¹³CO⁺, and CH₃OH emission lines. This component has a half-shell like appearance in the panels with $V_{c,LSR} = -82.5$ to -62.5 km s^{-1} of these emission lines. As mentioned above, the prominent component in the CH₃OH emission line suggests that the cloud is farther from Sgr A*. The component would be independent from the CND. Because the intensity ratio of SiO/H¹³CO⁺ is 3 – 4 in the component, shocked molecular gas is likely abundant in it. This component has no counterpart in the H42 α recombination line (see Figure 1-f), indicating no ionized gas in it. The component is called -80 km s⁻¹ molecular cloud (-80MC) hereafter.

3.2.6 -70 km s⁻¹ molecular cloud

The panels with $V_{c,LSR} = -82.5$ to -52.5 km s^{-1} in the CS emission line show that a molecular cloud is located around $l \sim 359.969^\circ, b \sim -0.030^\circ$. Although this component is also identified clearly in the

channel maps of the $C^{34}S$ emission line, it is faint in the SiO , $H^{13}CO^+$, and CH_3OH emission lines. This component has no counterpart in the $H42\alpha$ recombination line (see Figure 1-f), indicating no ionized gas in it. The component is called -70 km s^{-1} molecular cloud ($-70MC$) hereafter.

4 Discussion

4.1 Kinematics of the Circum-Nuclear Disk

As mentioned in Introduction, many previous works have shown that the CND is a torus-like molecular gas with the inner boundary radius of $r_{in} \sim 1.5 - 1.6 \text{ pc}$ with a rotation velocity of $V_{rot} \sim 100 - 120 \text{ km s}^{-1}$ around Sgr A* (e.g. Güsten et al. 1987; Jackson et al. 1993; Christopher et al. 2005; Montero-Castaño et al. 2009; Martín et al. 2012). In addition the velocity of the radial motion in the CND also has been estimated to be $\bar{V}_{rad} \sim 20 - 50 \text{ km s}^{-1}$ in their works. However the observed kinematics of the CND has not been fully explained only by the rotation with radial motion, and the outer boundary has not been clarified.

The inner radius of the CND is estimated to be $R_{in} \sim 1.5 \text{ pc}$ from the appearances in the moment 0 maps (see Figures 8a, 8c, 8e and 8g) and the channel maps in the $CS J = 2 - 1$, $SiO v = 0, J = 2 - 1$, $H^{13}CO^+ J = 1 - 0$, and $CS J = 7 - 6$ emission lines (see Figures 2, 4, 5 and 7). There are many outer components which do not obey the rotation law with radial motion in the position-velocity diagrams (see Figure 8) besides the anomalies mentioned in the previous section. The outer components are distributed mainly in the velocity range of $V_{LSR} \sim -30 \text{ to } +70 \text{ km s}^{-1}$ (see Figure 8). These components would not belong to the CND (see Figures 2, 4, 5 and 7) because they are identified to be large features outside the CND, for example, “Northeast Arm”, “Linear Filament” and so on; they have been recognize as parts of the CND in the previous observations (e.g. Montero-Castaño et al. 2009; Martín et al. 2012). In this case, the outer radius is estimated to be as small as $R_{out} \sim 2 \text{ pc}$. The inclination angle of the CND is estimated to be $i \sim 30 \pm 5^\circ$ ($i = 0^\circ$ for an edge-on ring) from the aspect ratios of the appearances of the CND in the moment 0 maps.

The kinematics of the CND is shown in the position-velocity diagrams along the major axis in the $CS J = 2 - 1$, $SiO v = 0, J = 2 - 1$, $H^{13}CO^+ J = 1 - 0$, and $CS J = 7 - 6$ emission lines (see Figures 8b, 8d, 8f, and 8h). Because the CND is not clear in the CH_3OH emission line as mentioned in the subsection 3.1, the position-velocity diagram is not shown here. The CND is identified as a series of components which are roughly along an inclined line in the diagrams (broken line parallelograms). These have been observed in the previous observations (e.g. Montero-Castaño et al. 2009; Martín et al. 2012). From the position-velocity diagrams (see Figures 8b, 8d, 8f, and 8h), the rotation velocity and radial motion of the CND are estimated to be $V_{rot} \sim \frac{100}{\cos i} = 115 \pm 10 \text{ km s}^{-1}$ and $V_{rad} \sim$

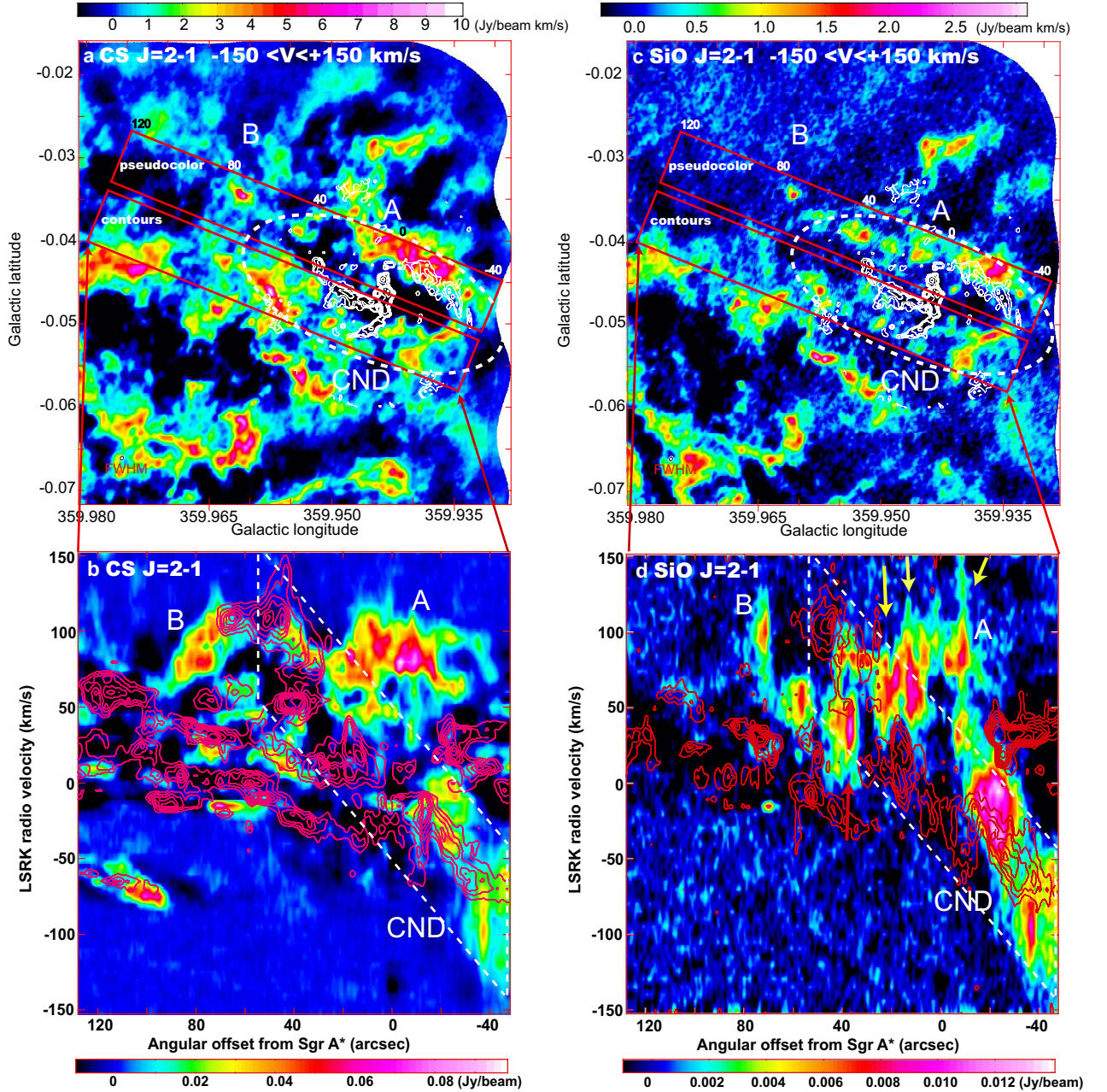


Fig. 8. **a** Moment 0 map in the CS $J = 2 - 1$ emission line as the finding chart of the CND (white-dashed ellipse). The contours in the finding charts show the continuum emission of the “Galactic Center Mini-spiral (GCMS)” at 100 GHz for comparison (Tsuboi et al. 2016). They are set at 3.75, 7.5, 15, 30, 60, 120, 240, 480, and 960 mJy beam⁻¹. **b** Position-velocity (P-V) diagram along the major axis of the CND in the CS $J = 2 - 1$ emission line. The sampling areas of the diagrams are shown as the red rectangles in the finding chart. The pseudo color and contours show the components in the northern and southern areas, respectively. The contour levels are set at 10.3, 20.6, 30.9, 41.2, 51.5, 61.8, and 82.4 mJy beam⁻¹. The white-dashed parallelogram indicates the CND conventionally identified in the P-V diagram (e.g. Güsten et al. 1987; Jackson et al. 1993; Christopher et al. 2005; Montero-Castaño et al. 2009; Martín et al. 2012). “A” and “B” indicate the anomalies A and B of the CND shown in Figures 2, 3, 4, 5, and 6. **c** Moment 0 map in the SiO $v = 0, J = 2 - 1$ emission line as the finding chart of the CND (white-dashed ellipse). **d** P-V diagram along the major axis of the CND in the SiO $v = 0, J = 2 - 1$ emission line. The contour levels are set at 2, 4, 6, 8, 10, 12, and 16 mJy beam⁻¹.

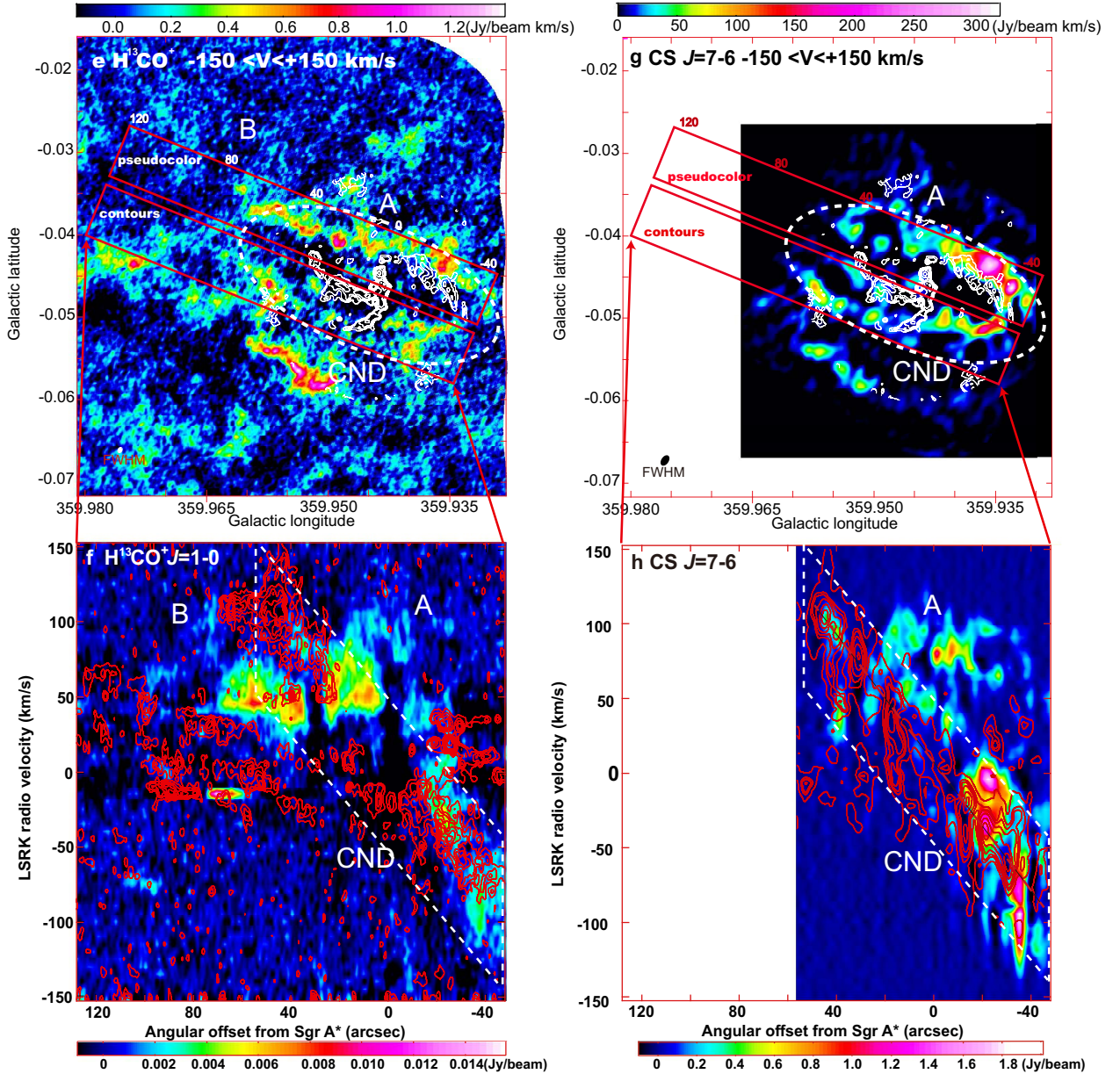


Fig. 8. Continued. **e** Moment 0 map in the $\text{H}^{13}\text{CO}^+ J = 1 - 0$ emission line as the finding chart of the CND (white-dashed ellipse). The contours in the finding charts show the continuum emission of the “Galactic Center Mini-spiral (GCMS)” at 100 GHz for comparison (Tsuboi et al. 2016). They are set at 3.75, 7.5, 15, 30, 60, 120, 240, 480, and 960 mJy beam^{-1} . **f** P-V diagram along the major axis of the CND in the $\text{H}^{13}\text{CO}^+ J = 1 - 0$ emission line. The contour levels are set at 1.1, 2.2, 3.3, 4.4, 5.5, 6.6, and 8.8 mJy beam^{-1} . **g** Moment 0 map in the CS $J = 7 - 6$ emission line as the finding chart of the CND (white-dashed ellipse). **h** P-V diagram along the major axis of the CND in the CS $J = 7 - 6$ emission line. The contour levels are set at 0.2, 0.4, 0.6, 0.8, 1.0, 1.2, and 1.6 Jy beam^{-1} .

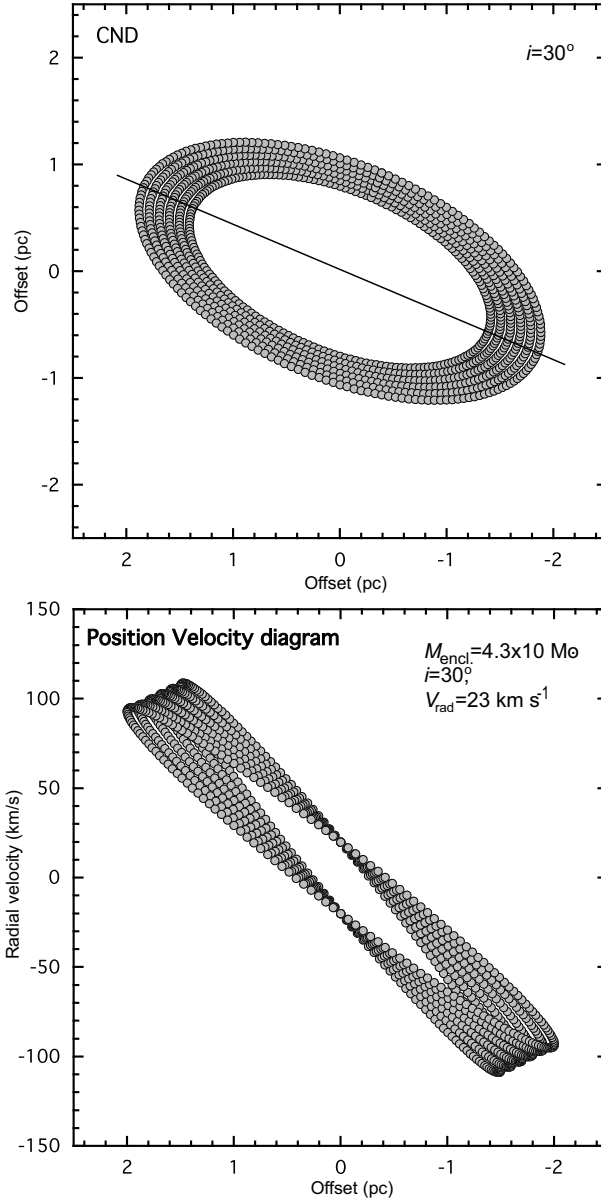


Fig. 9. **upper panel** Trajectories of the Keplerian motions with the enclosed mass of $4.3 \times 10^6 M_{\odot}$, the radius of $1.5 - 2.0$ pc, and the eccentricity of 0 and the radial motion of 23 km s^{-1} . The inclination angle is $i = 30^{\circ}$. **lower panel** Position velocity diagram of the trajectories along their major axis.

$\frac{20}{\cos i} = 23 \pm 5 \text{ km s}^{-1}$, respectively. The derived values are consistent with those in the previous observations (e.g. Güsten et al. 1987; Marr, Wright, & Backer 1993; Montero-Castaño et al. 2009; Martín et al. 2012). Figure 9 shows the Keplerian orbit with the derived inner radius, outer radius, inclination angle and radial motion. The enclosed mass of $4.3 \times 10^6 M_{\odot}$ reproduces the observed position-velocity diagrams.

4.2 Physical Properties of the Circum-Nuclear Disk

It has been reported that the moderately dense molecular gas in the CND with $\log N_{\text{H}_2} \sim 4.5$ has the kinetic temperatures of $T_{\text{K}} \sim 200$ K and the slightly denser gas with $\log N_{\text{H}_2} \sim 5.5$ has the kinetic temperatures of $T_{\text{K}} \sim 300 - 500$ K (Requena-Torres et al. 2012). It also has been reported that the CND would be dominated by the former component. The kinetic temperature of the molecular gas including CS molecules is assumed to be $T_{\text{K}} = 200$ K here.

We calculate the brightness and excitation temperatures of the CS $J = 2 - 1$ and CS $J = 7 - 6$ emission lines using the RADEX LVG program (Van der Tak et al. 2007) to estimate the physical properties of the CND. Figure 10a shows the relations of the CS $J = 2 - 1$ brightness temperature, $T_{\text{B}}(\text{CS } J = 2 - 1)$, and the brightness temperature ratio, $T_{\text{B}}(\text{CS } J = 7 - 6)/T_{\text{B}}(\text{CS } J = 2 - 1)$, on the plane of H_2 number density versus CS fractional abundance per velocity gradient are calculated at $T_{\text{K}} = 200$ K. Figure 10b shows the excitation temperatures of CS $J = 2 - 1$ and CS $J = 7 - 6$ emission lines, $T_{\text{ex}}(\text{CS } J = 2 - 1)$ and $T_{\text{ex}}(\text{CS } J = 7 - 6)$, on the same plane. The observed intensity peaks of the CS $J = 2 - 1$ brightness temperature in the CND and Anomaly A are plotted in the figures as the filled and open circles, respectively. They are clearly separated in the figure. This indicates that the physical properties of CND and AA are different from each other.

In figure 10b, the data points of the CND are distributed above the boundary where the excitation temperature of the CS $J = 2 - 1$ emission line is equal to the kinetic temperature. The calculated excitation temperature often has a negative sign, which nominally indicates that the emission is a maser one. However, this is likely an artifact made by a simplified velocity structure. Because the CS spectra in the CND do not show very high and very narrow profiles typical in the maser emission, it is reasonable that the $J = 2$ level of the CS molecules is thermalized. Then we consider that the excitation temperature is equal to the kinetic temperature of $T_{\text{K}} = 200$ K assumed above. On the other hand, the excitation temperature of the CS $J = 7 - 6$ emission line in the CND is in the range of $T_{\text{ex}}(\text{CS } J = 7 - 6) = 18 - 25$ K. This indicates that the $J = 7$ level of the CS molecules is sub-thermally excited. In addition, the excitation temperatures of the CS $J = 2 - 1$ and CS $J = 7 - 6$ emission lines in AA are in the ranges of $T_{\text{ex}}(\text{CS } J = 2 - 1) = 56 - 200$ K and $T_{\text{ex}}(\text{CS } J = 7 - 6) = 16 - 20$ K, respectively.

In figure 10a, the mean H_2 number density and CS fractional abundance per velocity gradient of the CND are estimated to be $n_{\text{H}_2} \sim 2.2 \times 10^5 \text{ cm}^{-3}$ and $\log[X(\text{CS})(\frac{dV}{dr})^{-1}] \sim -10.8$, respectively. Assuming that the CS fractional abundance and the velocity width of the CS emission line are $X(\text{CS}) = 10^{-8}$ and $\Delta V = 50 \text{ km s}^{-1}$, the path length of the molecular gas is estimated to be $\Delta l \sim 0.1 \text{ pc}$ by $X(\text{CS})(\frac{dV}{dr})^{-1} \sim X(\text{CS})(\frac{\Delta l}{\Delta V})$. The molecular column density based on the LVG

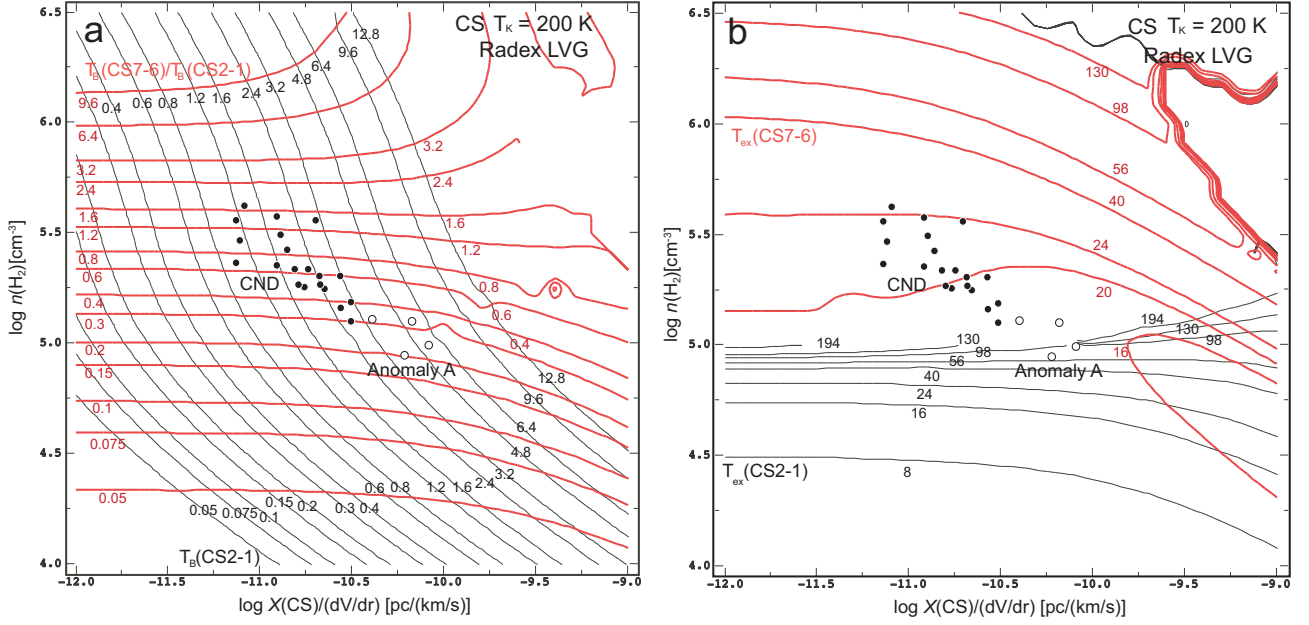


Fig. 10. a Relation of $T_B(\text{CS } J = 2 - 1)$ (black contours) vs $T_B(\text{CS } J = 7 - 6)/T_B(\text{CS } J = 2 - 1)$ (red contours) at $T_K = 200$ K, calculated by the RADEX LVG program (Van der Tak et al. 2007). The observed intensity peaks of the CS $J = 2 - 1$ brightness temperature in the the CND and Anomaly A are plotted as filled and open circles, respectively. **b** Excitation temperatures of CS $J = 2 - 1$ (black contours) and CS $J = 7 - 6$ (red contours) emission lines at $T_K = 200$ K.

model is derived to be $N_{\text{LVG}}(\text{H}_2) \sim n_{\text{H}_2} \times \Delta l = 7 \times 10^{22} \text{ cm}^{-2}$.

4.3 Molecular Gas Mass of the Circum-Nuclear Disk

The molecular gas mass of the CND would be key information to understand the origin of the CND. In the previous observations, the molecular gas mass of the CND had been derived based on dust continuum emission maps or integrated intensity maps of molecular emission lines, because the CND is identified easily as a ring-like feature surrounding Sgr A* in these maps. However, the velocity-resolved analysis has been hard to perform owing to the lack of sensitivity. The molecular gas mass of the CND even in the recent dust observations is scattered widely from $M = 0.6 \times 10^3 M_\odot$ to $5 \times 10^4 M_\odot$; $0.6 \times 10^3 M_\odot$ by SOFIA (Lau et al. 2013), $1 - 2 \times 10^4 M_\odot$ by SMA (Liu et al. 2013), $2 \times 10^4 M_\odot$ by JCMT (e.g. Oka et al. 2011), and $5 \times 10^4 M_\odot$ by Hershel (Etxaluze et al. 2011). On the other hand, the molecular gas mass of the CND derived from molecular emission line observations has been not well determined although a larger mass of $M = 1 - 3 \times 10^5 M_\odot$ has been reported (Smith&Wardle 2013). Because these works have different integration areas for the CND, the various CND masses do not always mean the ambiguity of the derivation method. It is still necessary to examine the derivation method of the molecular gas mass and to clarify what is the boundary of the CND. The later has been done in the subsection 4.1.

4.3.1 CS $J = 2 - 1$ and C³⁴S $J = 2 - 1$ emission lines

Using the line intensities of the CS and C³⁴S emission lines, we derive the molecular gas mass of the CNL. In that case, the ambiguity of the optical thickness of the CS emission line leads to the uncertainty of the molecular gas mass. If the abundance ratio of CS molecule to C³⁴S molecule is equal to the typical cosmic ratio of the isotopes of S, $\frac{X(\text{S})}{X(\text{C}^{34}\text{S})} = \frac{X(\text{CS})}{X(\text{C}^{34}\text{S})} = 22.35$ (https://physics.nist.gov/cgi-bin/Compositions/stand_alone.pl), and the C³⁴S emission line is optically thin, the optical thickness of the CS emission line τ , is estimated from the line intensity ratio of the CS and C³⁴S emission lines as follows;

$$\frac{I(\text{CS})}{I(\text{C}^{34}\text{S})} = \frac{f(\text{CS})T_{\text{ex}}(\text{CS})(1 - e^{-\tau})}{f(\text{C}^{34}\text{S})T_{\text{ex}}(\text{C}^{34}\text{S})(1 - e^{-\frac{\tau}{22.35}})}. \quad (1)$$

Here the integrated line intensities of CS and C³⁴S are $I(\text{CS}) = \int I_{\nu,\text{CS}}(v)dv$ and $I(\text{C}^{34}\text{S}) = \int I_{\nu,\text{C}^{34}\text{S}}(v)dv$, respectively. The components belonging to the CNL are identified in the channel maps by the criteria shown in the previous section (the white-dashed ellipse and the white-dashed parallelogram in Figure 8). The line intensities are calculated for the individual components. $f(\text{CS})$ and $f(\text{C}^{34}\text{S})$ are the beam filling factors of the CS and C³⁴S emission lines, respectively, and they are assumed to be identical here, $f(\text{CS}) = f(\text{C}^{34}\text{S})$. The derived optical thicknesses of the CS emission line are up to $\tau \lesssim 2$ assuming that $T_{\text{ex}}(\text{CS}) = T_{\text{ex}}(\text{C}^{34}\text{S})$. Using an optical thickness correction factor, $\tau(v)/(1 - e^{-\tau(v)})$, the corrected line intensity of the CS $J = 2 - 1$ emission line is given by

$$I_{\text{corr.}}(\text{CS}) = \int I_{\nu,\text{CS}}(v) \frac{\tau(v)}{1 - e^{-\tau(v)}} dv. \quad (2)$$

The LTE molecular column density from the CS $J = 2 - 1$ emission line is given by

$$N_{\text{LTE}}(\text{H}_2)[\text{cm}^{-2}] = \frac{2.35 \times 10^{13} e^{\frac{2.35}{T_{\text{ex}}}} I_{\text{corr.}}(\text{CS})/\Omega_{\text{beam}}[\text{Jy beam}^{-1} \text{ km s}^{-1}]}{X(\text{CS})(1 - e^{-\frac{4.7}{T_{\text{ex}}}})}. \quad (3)$$

Here the Einstein A coefficient of the CS $J = 2 - 1$ emission line is assumed to be $A_{21} = 2.2 \times 10^{-5} \text{ s}^{-1}$. The excitation temperature of the CS $J = 2 - 1$ emission line is estimated to be $T_{\text{ex}} = 200 \text{ K}$ in the previous subsection using the RADEX LVG program (Van der Tak et al. 2007). The fractional abundance of the CS molecule is assumed to be $X(\text{CS}) = \frac{N(\text{CS})}{N(\text{H}_2)} = 1 \times 10^{-8}$, which is usually used for molecular clouds in the disk region. The LTE molecular column density is approximately given by

$$N_{\text{LTE}}(\text{H}_2)[\text{cm}^{-2}] \simeq 5.1 \times 10^{20} T_{\text{ex}} I_{\text{corr.}}(\text{CS})/\Omega_{\text{beam}}[\text{Jy beam}^{-1} \text{ km s}^{-1}]. \quad (4)$$

Note that the column density is proportion to T_{ex} . The typical LTE molecular column density of the CNL is $N_{\text{LTE}}(\text{H}_2) \sim 1 \times 10^{23} (T_{\text{ex}}/200) \text{ cm}^{-2}$. This is consistent with the typical molecular column density based on the LVG model, $N_{\text{LTE}}(\text{H}_2) \sim 7 \times 10^{22} \text{ cm}^{-2}$, as mentioned in the previous subsection. Finally, the LTE molecular gas mass is given by

$$M_{\text{LTE}}[M_{\odot}] = \mu[M_{\odot}]A_{\text{beam}}[\text{cm}^2]\Sigma N_{\text{H}_2, \text{LTE}} = 14.6(T_{\text{ex}}/200)\Sigma I_{\text{corr.}}(\text{CS}), \quad (5)$$

where μ is the mean molecular weight per H_2 molecule: $\mu = 2.8$ in amu $= 2.4 \times 10^{-57} M_{\odot}$, and A_{beam} is the physical area corresponding to the beam size of Ω_{beam} : $A_{\text{beam}} = 5.97 \times 10^{34} \text{cm}^2$ for the $2.3'' \times 1.6''$ beam.

The total corrected integrated line intensity in the CND of the CS $J = 2 - 1$ emission line is $\Sigma I_{\text{corr.}}(\text{CS}) = 2.1 \times 10^3 \text{ Jy km s}^{-1}$, whereas that of the C^{34}S $J = 2 - 1$ emission line is $\Sigma I(\text{C}^{34}\text{S}) = 8.8 \times 10^1 \text{ Jy km s}^{-1}$. The total velocity range is from -150 to 150 km s^{-1} in V_{LSR} for both emission lines. The mean line intensity ratio of the CND is calculated to be $\frac{\Sigma I_{\text{corr.}}(\text{CS})}{\Sigma I(\text{C}^{34}\text{S})} \sim 16.7$. Then the typical optical thickness of the CS emission line of the CND is estimated to be $\bar{\tau}(\text{CND}) \sim 0.63$ whereas that of AA is as large as $\bar{\tau}(\text{AA}) \sim 1.5$. The LTE molecular gas mass of the CND is derived to be $M_{\text{LTE}}(\text{CND}) = 3.1 \times 10^4 (T_{\text{ex}}/200) M_{\odot}$. The LTE mass is consistent with those derived in the previous observations mentioned above. In addition, the LTE molecular gas masses of AA, AB, and AC are derived to be $M_{\text{LTE}}(\text{AA}) = 1.3 \times 10^4 (T_{\text{ex}}/200) M_{\odot}$, $M_{\text{LTE}}(\text{AB}) = 7.0 \times 10^3 (T_{\text{ex}}/200) M_{\odot}$, and $M_{\text{LTE}}(\text{AC}) = 1.0 \times 10^3 (T_{\text{ex}}/200) M_{\odot}$, respectively. However, the excitation temperature for these components may be lower than $T_{\text{ex}} = 200 \text{ K}$ (see figure 10b).

We also derive the LTE molecular gas mass of the CND based on the data of the CS $J = 7 - 6$ emission line by the same procedure for comparison. The integrated line intensity in the CND of the CS $J = 7 - 6$ emission line is $\Sigma I(\text{CS } J = 7 - 6) = 4.8 \times 10^5 \text{ Jy km s}^{-1}$. Here the Einstein A coefficient of the CS $J = 7 - 6$ emission line is assumed to be $A_{76} = 0.8 \times 10^{-3} \text{ s}^{-1}$. The excitation temperature of the CS $J = 7 - 6$ emission line is calculated to be $T_{\text{ex}} = 18 - 25 \text{ K}$ using the RADEX LVG program (Van der Tak et al. 2007) as mentioned in the previous subsection (see figure 10b). Then the LTE molecular gas mass derived from the CS $J = 7 - 6$ emission line becomes $M_{\text{LTE}}(\text{CND}) = 1.5 \times 10^4 (T_{\text{ex}}/22) M_{\odot}$.

4.3.2 $\text{H}^{13}\text{CO}^+ J = 1 - 0$ emission line

We derive the LTE molecular gas mass of the CND based on the observation in the H^{13}CO^+ emission line by the same procedure (see Figure 5). We consider that the $J = 1$ level of the H^{13}CO^+ molecules is also thermalized and the excitation temperature is equal to the kinetic temperature of $T_{\text{K}} = 200 \text{ K}$. The Einstein A coefficient of the H^{13}CO^+ emission line is assumed to be $A_{10} = 3.9 \times 10^{-5} \text{ s}^{-1}$.

The integrated line intensity in the CND of the H^{13}CO^+ emission line is $\Sigma I(\text{H}^{13}\text{CO}^+) = 9.2 \times 10^1 \text{ Jy km s}^{-1}$. Then the LTE molecular gas mass of the CND from the H^{13}CO^+ emission line observation is derived to be $M_{\text{LTE}} = 1.5 \times 10^4 (T_{\text{ex}}/200) M_{\odot}$ assuming the fractional abundance of the H^{13}CO^+ molecule of $X(\text{H}^{13}\text{CO}^+) = \frac{N(\text{H}^{13}\text{CO}^+)}{N(\text{H}_2)} = 4 \times 10^{-10}$ (for the CND; Amo-Baladr3n, Mart3n-Pintado & Mart3n 2011). Although the fractional abundance for the CND is nine times larger than

Table 1. Physical Parameters of the Circum-Nuclear Disk and Tidally-disrupted Molecular Clouds

Object	$\tau(\text{CS}2-1)$	$M_{\text{LTE}}(\text{CS}2-1)^1$	$M_{\text{LTE}}(\text{H}^{13}\text{CO}^+)^2$	$M_{\text{LTE}}(\text{CS}7-6)^3$
		$[M_{\odot}]$	$[M_{\odot}]$	$[M_{\odot}]$
CND	~ 0.63	$3.1 \times 10^4 (T_{\text{ex}}/200)$	$1.5 \times 10^4 (T_{\text{ex}}/200)$	$1.5 \times 10^4 (T_{\text{ex}}/22)$
Anomaly A	~ 1.5	$1.3 \times 10^4 (T_{\text{ex}}/200)$	$2.3 \times 10^3 (T_{\text{ex}}/200)$	–
Anomaly B	~ 0.18	$7.0 \times 10^3 (T_{\text{ex}}/200)$	$2.7 \times 10^3 (T_{\text{ex}}/200)$	–
Anomaly C	~ 3.2	$1.0 \times 10^3 (T_{\text{ex}}/200)$	–	–

¹ We assumed $A_{21} = 2.2 \times 10^{-5} \text{ s}^{-1}$ and $X(\text{CS}) = 1 \times 10^{-8}$.

² We assumed $A_{10} = 3.9 \times 10^{-5} \text{ s}^{-1}$ and $X(\text{H}^{13}\text{CO}^+) = 4 \times 10^{-10}$ (Amo-Baladr3n, Mart3n-Pintado & Mart3n 2011).

³ We assumed $A_{76} = 0.8 \times 10^{-3} \text{ s}^{-1}$ and $X(\text{CS}) = 1 \times 10^{-8}$.

that for the Orion A molecular cloud, $X(\text{H}^{13}\text{CO}^+) = 5 \times 10^{-11}$ (Ikeda, Sunada, & Kitamura 2007), the consistency in the derived gas masses from the CS and H^{13}CO^+ observations suggests that the estimations of the excitation temperature and the fractional abundance are good for the CND.

The LTE masses of the CND derived from the CS $J = 7 - 6$ and $\text{H}^{13}\text{CO}^+ J = 1 - 0$ emission lines, $M_{\text{LTE}} \sim 1.5 \times 10^4 (T_{\text{ex}}/200) M_{\odot}$, are half of that derived from the CS $J = 2 - 1$ emission line, $M_{\text{LTE}} \sim 3.1 \times 10^4 (T_{\text{ex}}/200) M_{\odot}$. These relations are consistent with that the effective critical densities of the CS $J = 7 - 6$ and $\text{H}^{13}\text{CO}^+ J = 1 - 0$ emission lines, $n_{\text{eff}} \sim 10^5 \text{ cm}^{-3}$, are higher than that of the CS $J = 2 - 1$ emission line, $n_{\text{eff}} \sim 10^3 \text{ cm}^{-3}$. The derived masses of tidally disrupted molecular clouds which will be discussed in the next subsection are also summarized in Table 1.

4.4 Tidally-disrupted Molecular Clouds falling to the Galactic Center

AA, AB, and AC could be clouds falling from the outer regions onto the CND or the GCMS because they apparently connect with the inner structures. The channel maps with $V_{\text{c,LSR}} = 77.5$ to 117.5 km s^{-1} in the CS emission line show that AA has a continuous appearance from the northeast to the vicinity of WA (see Figure 2). Although the northeastern part of AA is prominent in the CH_3OH emission line, the inner part apparently adjacent to WA is faint in the emission line (see the channel maps with $V_{\text{c,LSR}} = 77.5$ to 97.5 km s^{-1} in the CH_3OH emission line in Figure 6). On the other hand, although the northeastern part is faint in the SiO emission line, the inner part is prominent in the emission line (see Figure 4). The part is also identified by SOFIA as a compact component in extremely high- J CO emission lines (up to $J = 16 - 15$) (Requena-Torres et al. 2012). Because the CH_3OH emission line is activated by shock with milder shock velocity, $\Delta V \sim 10 \text{ km s}^{-1}$, than that of the SiO emission line, the northeastern part is abundant in mildly shocked molecular gas. The SiO enhancement shows that the inner part is abundant in strongly shocked molecular gas. It is likely that

the CH₃OH emission line of the inner part is also enhanced by the shock, but the observed weak line suggests the depletion of the CH₃OH molecules in the inner part.

AA has wide velocity and narrow sub-features in the PV diagram of the SiO emission line (arrows in figure 8). These are also identified in the channel maps of the SiO emission line (see figure 4). These properties suggest that there are several spots including abundant strongly shocked molecular gas in AA. Because there is no counterpart of the ionized gas, these would be activated by C-type shocks. The FWHM velocity widths of the components in the SiO emission line are up to $\Delta V_{\text{FWHM}} = 50 \text{ km s}^{-1}$. This may be interpreted as the shock velocity between the approaching gas and the CND, $V_{\text{shock}} \sim 50 \text{ km s}^{-1}$. The magnetic field strength around the CND is as strong as $B \sim 4 \text{ mG}$, which was estimated by the Zeeman effect of the OH maser line (Yusef-Zadeh et al. 1996). While the Alfvén velocity in molecular material is given by

$$V_A [\text{km s}^{-1}] \sim 1300 \times B [\text{mG}] / \sqrt{n(\text{H}_2) [\text{cm}^{-3}]}, \quad (6)$$

when the molecules are assumed to be frozen in the magnetic field. Based on the LVG model, the number density of AA is as high as $n(\text{H}_2) \sim 0.6 - 1.2 \times 10^5 \text{ cm}^{-3}$ (see figure 10b). The Alfvén velocity is estimated to be $V_A \sim 15 - 20 \text{ km s}^{-1}$. Because the Alfvén velocity is as large as the shock velocity, it is plausible that the shock wave becomes C-type.

The CH₃OH molecule is reported to be destroyed easily through the cosmic-ray photodissociation reaction in the vicinity of Sgr A*; $\text{CH}_3\text{OH} + \text{c.r.} \rightarrow \text{H}_2\text{CO} + \text{H}_2$ (Harada et al. 2015). The disappearance of AA in the CH₃OH emission line suggests that the inner part of AA is really located near Sgr A* rather than chance coincident. We argue that AA is falling from the outer region to the CND, being disrupted by the tidal shear of Sgr A* and affected by cosmic-ray. AA is probably a route of feeding molecular gas to the CND. If this is the case, it is possible that the falling cloud does not obey the rotation law of the CND as observed because the orbit depends on the initial conditions including impact parameter and the conditions would be various. The molecular cloud would be being fallen currently from the outer region to the CND because the dynamical relaxation by collisions with molecular gas in the CND has not yet occurred. In addition, the photodissociation by cosmic-ray is probably why it is hard to depict the CND itself in the CH₃OH emission line (see Figure 1-e).

Figure 11 shows the positional relation between the molecular gas of AB in the CS emission line and the ionized gas of Eastern Arm (EA) in the H42 α recombination line. The ionized gas motion in EA has been explained as a part of a Keplerian elliptical orbit which is determined by the appearance and kinematics (e.g. Zhao et al. 2009; Zhao et al. 2010; Tsuboi et al. 2017). AB and EA are identified as a continuous and united body although they are made of the different gas components,

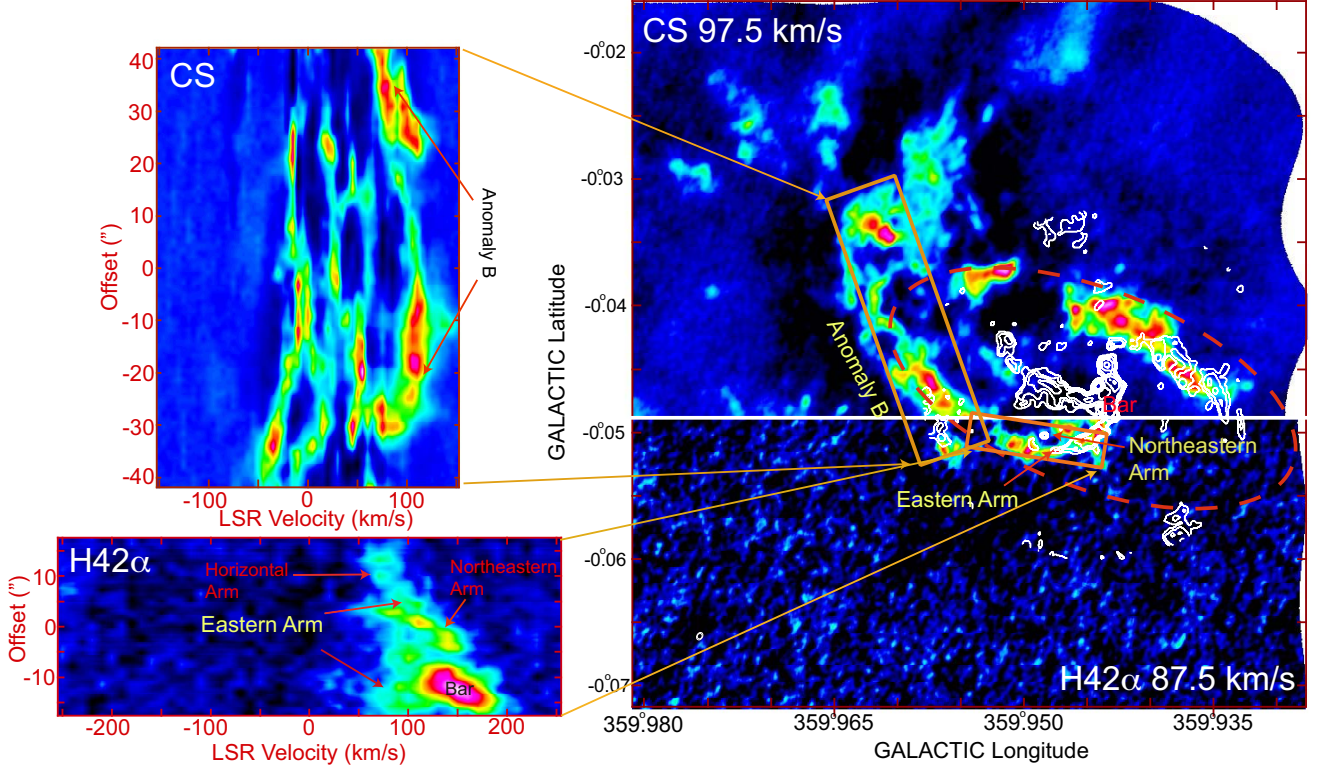


Fig. 11. Right panel: Integrated intensity map of Anomaly B at $V_{\text{LSR}} = 97.5 \text{ km s}^{-1}$ in the CS $J = 2 - 1$ emission line (upper part) and Eastern Arm at $V_{\text{LSR}} = 87.5 \text{ km s}^{-1}$ in the H42 α recombination line (lower part). The central velocities are shown at the upper left and lower right corners of the upper and lower parts, respectively. The velocity widths of the two parts are 10 km s^{-1} . The red dashed ellipse shows the elliptical outline of the CND. The white contours show the continuum emission at 100 GHz of the “Galactic Center Mini-spiral” at 100 GHz for comparison (Tsuboi et al. 2016). Upper left panel: PV diagram along Anomaly B in the CS $J = 2 - 1$ emission line. The sampling area is shown by the upper red rectangle in the right panel. Lower left panel: PV diagram along Eastern Arm in the H42 α recombination line. The sampling area is shown by the lower red rectangle in the right panel.

Because a compact component is seen in the SiO emission line around the boundary between AB and EA (see Figure 4), the molecular gas may have been ionized by strong UV emission from the Central Cluster and compressed by the expanding ionized gas. The area is also identified by SOFIA as a compact component in extremely high- J CO emission lines (up to $J = 16 - 15$) (Requena-Torres et al. 2012). On the other hand, the other area of AB is not clear in the SiO emission line. As mentioned in the subsection 3.2.2, AB has filamentary substructures. The interactions between the filaments may produce mildly shocked molecular gas ($\Delta \sim 10 \text{ km s}^{-1}$). Therefore, almost all part of AB is not abundant in strongly shocked molecular gas except for the boundary area. Meanwhile the northern half of AB can be also identified in the channel maps with $V_{\text{c,LSR}} = 77.5$ to 97.5 km s^{-1} in the CH₃OH emission line. The northern half of AB is abundant in mildly shocked molecular gas. Therefore the shock velocity in the structure is probably in the range of 10 to 30 km s^{-1} . The southern half of AB cannot be identified in the channel maps of $V_{\text{c,LSR}} = 107.5$ and 117.5 km s^{-1} except for the small patch located around $l \sim 359.960^\circ, b \sim -0.034^\circ$ (see Figure 6). Consequently, we argue that

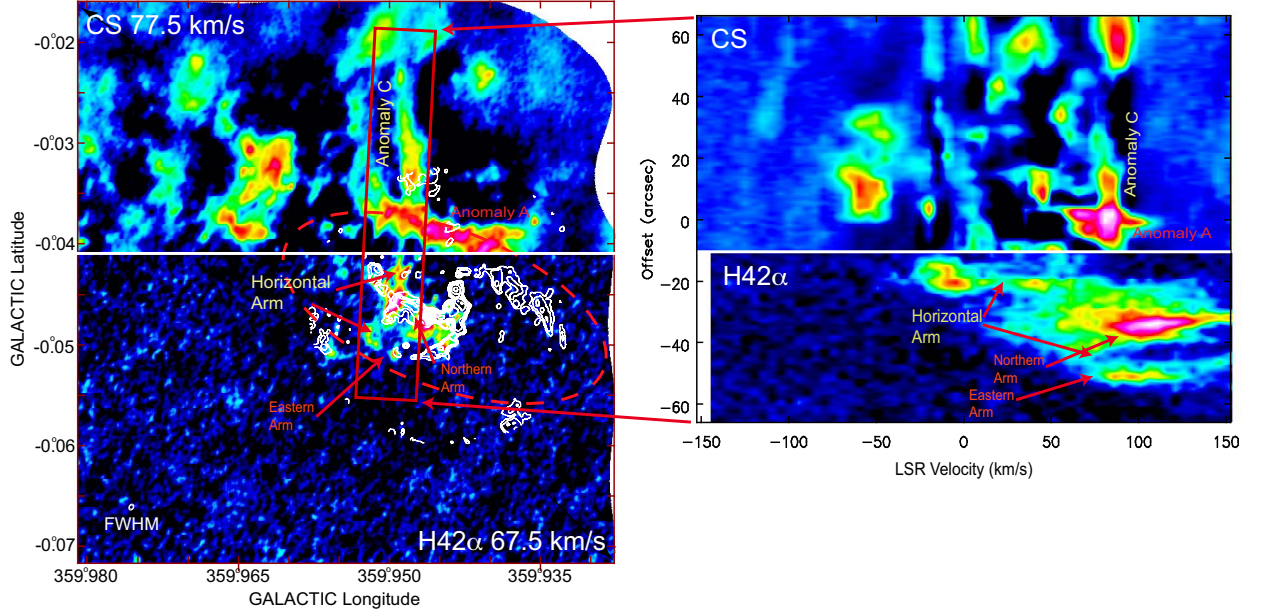


Fig. 12. Left panel: Integrated intensity map of Anomaly C at $V_{\text{LSR}} = 77.5 \text{ km s}^{-1}$ in the CS $J = 2 - 1$ emission line (upper part) and Horizontal Arm at $V_{\text{LSR}} = 67.5 \text{ km s}^{-1}$ in the H42 α recombination line (lower part). The central velocities are shown at the upper left and lower right corners of the upper and lower parts, respectively. The velocity widths of the two parts are 10 km s^{-1} . The red dashed ellipse shows the elliptical outline of the CND. The white contours show the continuum emission at 100 GHz of the “Galactic Center Mini-spiral” at 100 GHz for comparison (Tsuboi et al. 2016). Upper right panel: PV diagram along Anomaly C in the CS $J = 2 - 1$ emission line. The sampling area is shown by the upper half of the red rectangle in the left panel. Lower right panel: PV diagram along Horizontal Arm in the H42 α recombination line. The sampling area is shown by the lower half of the red rectangle in the left panel.

AB is falling from the outer region to the vicinity of Sgr A*, being disrupted by the tidal shear of Sgr A* and affected by cosmic ray. When AB is further approaching to Sgr A*, it would be immediately ionized by extremely strong Lyman continuum emission ($\sim 4 \times 10^{50} \text{ s}^{-1}$) from the Central Cluster (e.g. Scoville et al. 2003). The final destination of the falling clouds depends on the initial conditions including impact parameter as mentioned above. Because AB is ionized and connects with EA, the impact parameter of AB is considered to be smaller than that of AA.

Figure 12 shows the positional relation between the molecular gas of AC in the CS emission line and the ionized gas of Horizontal Arm (HA) in the H42 α recombination line. HA is identified as a nearly vertical substructure of the ionized gas in the Galactic coordinates. AC and HA are apparently identified as a continuous and nearly vertical filament in the channel map. However, the AC is not continuous to HA in the position velocity diagram. This would be also a falling molecular gas from the outer region to the vicinity of Sgr A* but is not ionized. The impact parameter of AC seems larger than that of AB.

5 Conclusions

We present the high angular resolution and high sensitivity images of the CND and the surrounding region in the CS $J = 2 - 1$, SiO $v = 0$ $J = 2 - 1$, $\text{H}^{13}\text{CO}^+ J = 1 - 0$, $\text{C}^{34}\text{S } J = 2 - 1$, and $\text{CH}_3\text{OH } J_{K_a, K_c} = 2_{1,1} - 1_{1,0} A_{--}$ emission lines using ALMA.

- The CND is depicted as a torus-like molecular gas with the inner radius of $R_{\text{in}} \sim 1.5$ pc and the outer radius of $R_{\text{out}} \sim 2$ pc in these emission lines except for the CH_3OH emission line.
- The kinematics of the CND roughly obeys rotation with some radial motion. The rotation velocity and radial motion of the CND are estimated to be $V_{\text{rot}} \sim 115$ km s $^{-1}$ and $V_{\text{rad}} \sim 23$ km s $^{-1}$, respectively.
- The LTE molecular gas mass of the CND is estimated to be $M_{\text{LTE}} \sim 3.1 \times 10^4 M_{\odot}$ from the observations of the CS $J = 2 - 1$ and $\text{C}^{34}\text{S } J = 2 - 1$ emission lines.

Our derived size, kinematics, and mass of the CND are consistent with those in the previous observations.

We also found some anomalous molecular clouds in the surrounding region, which have filamentary appearances prominent in the CS $J = 2 - 1$ emission line.

- AA is positionally connected with the northwestern sector of the CND, which is adjacent to WA. This is likely being disrupted by the tidal shear of Sgr A * . The cloud seems to rotate around Sgr A * in the opposite direction to the CND. The molecular cloud would be recently falling from the outer region to the CND because the relaxation is not yet occurred.
- AB is continuously connected with the eastern tip of the “Eastern Arm (EA)” of the GCMS. The velocity of the cloud is consistent with that of the ionized gas in the EA. These facts suggest that the molecular cloud is falling from the outer region to the vicinity of Sgr A * , being disrupted by the tidal shear, and ionized by strong UV emission from the Central Cluster because the impact parameter of the cloud is smaller than that of AA.

These clouds would play an important role in transferring material from the outer region of the Sgr A complex to the CND and/or the vicinity of Sgr A * .

Acknowledgments

This work is supported in part by the Grant-in-Aid from the Ministry of Education, Sports, Science and Technology (MEXT) of Japan, No.16K05308. This work makes use of the following ALMA data: ADS/JAO.ALMA#2012.1.00080.S and ALMA#2012.1.00543.S. The later data are retrieved from the JVO portal (<http://jvo.nao.ac.jp/portal>) operated by the National Astronomical Observatory of Japan (NAOJ). The National Radio Astronomy Observatory (NRAO) is a facility of the National Science Foundation operated under cooperative agreement by Associated Universities, Inc. ALMA is a partnership of ESO (representing its member states), NSF (USA) and NINS (Japan), together with NRC (Canada), NSC and ASIAA (Taiwan), and

KASI (Republic of Korea), in cooperation with the Republic of Chile. The Joint ALMA Observatory is operated by ESO, AUI/NRAO and NAOJ. This work has made use of NASA's Astrophysics Data System.

References

- Amo-Baladrón, Martín-Pintado & Martín, 2011, *A&A*, 526, A54
- Boehle, A. et al. 2016, *ApJ*, 830, 17
- Christopher, M. H., Scoville, N. Z., Stolovy, S. R. & Yun, Min S. 2005, *ApJ*, 622, 346
- Ekers, R. D., van Gorkom, J. H., Schwarz, U. J., & Goss, W. M., 1983, *A&A*, 122, 143
- Etxaluze, M., Smith, H.A., Tolls, V., Stark, A. A., & González-Alfonso, E. 2011, *AJ*, 142, id.134
- Ghez, A. M., et al. 2008, *ApJ*, 689, 1044
- Gillessen, S., Eisenhauer, F., Trippe, S., Alexander, T., Genzel, R., Martins, F., & Ott, T. 2009, *ApJ*, 692, 1075
- Gusdorf, A., Cabrit, S., Flower, D.R., & Pineau des Forêts, G., 2008, *A&A*, 482, 809
- Güsten, R., Genzel, R., Wright, M. C. H., Jaffe, D. T., Stutzki, J., & Harris, A. I. 1987, *ApJ*, 318, 124
- Harada, N., Riquelme, D., Viti, S. et al. 2015, *A&A*, 584, A102
- Hartquist, T. W., Menten, K. M., Lepp, S., & Dalgarno, A. 1995, *MNRAS*, 272, 184
- Hsieh, P-Y., Koch, P. M., Ho, P. T. P., et al. 2017, *ApJ*, 847, id. 3
- Ikedo, N., Sunada, K., & Kitamura, Y., 2007, *ApJ*, 665, 1194
- Jackson, J. M., Geis, N., Genzel, R., Harris, A. I., Madden, S., Poglitsch, A., Stacey, G. J., & Townes, C. H., 1993, *ApJ*, 402, 173
- Jiménez-Serra, I., Caselli, Martín-Pintado, P.J., & Hartquist, T. W., 2008, *A&A*482, 549
- Lacy, J. H., Townes, C. H., Geballe, T. R., & Hollenbach, D. J. 1980. *ApJ*, 241, 132
- Lacy, J. H., Achtermann, J. M., & Serabyn, E. 1991, *ApJ*, 380, 71
- Lau, R. M., Herter, T. L., Morris, M. R., Becklin, E. E., & Adams, J. D. , 2013, *ApJ*, 775, 37
- Liu, H. B., Ho, P. T. P., Wright, Melvyn C. H. et al. 2013, *ApJ*, 770, id44
- Lo, K.Y. & Claussen, M. J., 1983, *Nature*, 306, 647
- Marr, J. M., Wright, M. C. H., & Backer, D. C. 1993, *ApJ*, 411, 667
- Martín, S., Martín-Pintado, J., Montero-Castaño, M., Ho, P. T. P., & Blundell, R. 2012, *A&A*, 539, id.A29
- McMullin, J. P., Waters, B., Schiebel, D., Young, W., & Golap, K. 2007, *Astronomical Data Analysis Software and Systems XVI (ASP Conf. Ser. 376)*, ed. R. A. Shaw, F. Hill, & D. J. Bell (San Francisco, CA: ASP), 127
- Montero-Castaño, M., Herrnstein, R. M. & Ho, P. T. P. 2009, *ApJ*, 695, 1477
- Oka, T., Nagai, M., Kamegai, K., & Tanaka, K. 2011, *ApJ*, 732, id. 120
- Reid, M. J., Menten, K. M., Genzel, R., Ott, T., Schödel, R., & Eckart, A. 2003, *ApJ*, 587, 208

Requena-Torres, M. A., Güsten, R., Weiß, A. et al. 2012, A&A, 542, id L21
Roberts, D. A., Yusef-Zadeh, F., & Goss, W. M. 1996, ApJ, 459, 627
Schödel, R., Merritt, D. & Eckart, A., 2009, A&A, 502, 91
Scoville, N. Z., Stolovy, S. R., Rieke, M., Christopher, M., & Yusef-Zadeh, F., 2003, ApJ, 594, 294
Serabyn, E. & Lacy, J. H. 1985, ApJ, 293, 445
Serabyn, E., Guesten, R., Walmsley, J. E., Wink, J. E., & Zylka, R. 1986, A&A, 169, 85
Serabyn, E., Lacy, J. H., Townes, C. H., & Bharat, R. 1988, ApJ, 326, 171
Shukla, H., Yun, M.S., Scoville, N.Z., 2004, ApJ, 616, 231
Smith, I. L. & Wardle, M. 2013, MNRAS, 437, 3159
Takekawa, S., Oka, T., & Tanaka, K., 2017, ApJ, 834, id 121
Tsuboi, M., Kitamura, Y., Miyoshi, M., Uehara, K., Tsutsumi, T., & Miyazaki, A., 2016, PASJ, 68, id. L7
Tsuboi, M., Kitamura, Y., Uehara, K., Miyawaki, R., Tsutsumi, T., Miyazaki, A., & Miyoshi, M., 2017, ApJ, 842, id. 94
Uehara, K., Tsuboi, M., Kitamura, Y., & Miyazaki, A., 2018, ApJ, submitted
Van der Tak, F.F.S., Black, J.H., Schöier, F.L., Jansen, D.J., & van Dishoeck, E.F., 2007, A&A, 468, 627
Wright, M. C. H., Coil, A. L., McGary, R. S., Ho, P. T. P. & Harris, A. I., 2001, ApJ, 551, 254
Yusef-Zadeh, F., Roberts, D. A., Goss, W. M., Frail, D. A., & Green, A. J. 1996, ApJ, 466, L25
Zhao, J-H, Morris, M. R. Goss, W. M. & Tao, A., 2009, ApJ, 699, 186
Zhao, J.-H., Blundell, R., Moran, J. M., Downes, D., Schuster, K. F., Marrone, D. P., 2010, ApJ, 723, 1097
Zylka, R., Mezger, P. G., & Wink, J. E., 1990, A&A, 234, 133